Surveys in Geophysics (2022) 43:1761–1791
https://doi.org/10.1007/s10712-022-09730-3

Acoustic and Electrical Properties of Tight Rocks: A Comparative Study Between Experiment and Theory

Mengqiang Pang[1,2] · Jing Ba[1] · José M. Carcione[1,3] · Martin Balcewicz[2] · Wenzheng Yue[4] · Erik H. Saenger[2,5,6]

Received: 10 April 2022 / Accepted: 1 July 2022 / Published online: 12 August 2022
© The Author(s), under exclusive licence to Springer Nature B.V. 2022

Abstract

The acoustic-electrical (AE) response of subsurface hydrocarbon reservoirs is highly affected by rock heterogeneity. In particular, the characterization of the microstructure of tight (low-permeability) rocks can be aided by a joint interpretation of AE data. To this purpose, we evaluate cores from a tight-oil reservoir to obtain the rock mineralogy and pore structure by X-ray diffraction and casting thin sections. Then, ultrasonic and resistivity experiments are performed under different confining pressures to analyze the effects of pores, microcracks and mineralogy on the AE properties. We have developed acoustic and electrical models based on effective-medium theories, and the Cole–Cole and triple-porosity equations, to simulate the response to total and soft (crack) porosities and clay content. The results show that these properties play a significant role. Then, a 3D rock-physical template is built and calibrated by using the core samples and well-log data. The template is applied to tight-oil reservoirs to estimate the rock properties, which are validated with log data. The good match between the predictions and these data indicates that the model can effectively explain the effects of the heterogeneous microstructure on the AE data.

Keywords Acoustic and electrical properties · Tight-oil rock · Microstructure · Heterogeneity · 3D rock physics template

✉ Jing Ba
jba@hhu.edu.cn

[1] School of Earth Sciences and Engineering, Hohai University, Nanjing 211100, China

[2] Hochschule Bochum, Am Hochschulcampus 1, Bochum 44801, Germany

[3] National Institute of Oceanography and Applied Geophysics – OGS, Borgo Grotta Gigante 42/c, Trieste, Sgonico 34010, Italy

[4] China University of Petroleum (Beijing), Beijing 100000, China

[5] Fraunhofer IEG - Institution for Energy Infrastructures and Geothermal Energy, Am Hochschulcampus 1, 44801 Bochum, Germany

[6] Institute of Geology, Mineralogy, and Geophysics, Ruhr-University Bochum, Universitätsstrasse 150, 44801 Bochum, Germany

Article Highlights

- Tight rock microstructure is analyzed with X-ray diffraction, thin sections and ultrasonic and electrical resistivity tests
- Rock acoustic-electrical properties are obtained by the effective-medium and triple-porosity theories
- Practical application is given based on an acoustic-electrical rock physics template

1 Introduction

With the depletion of conventional oil resources, tight-oil reservoirs become the next hydrocarbon prospects (Kathel and Mohanty 2013; Ghanizadeh et al. 2015; Behmanesh et al. 2018; Lin et al. 2022). Tight-oil rocks have a complex pore structure and mineral composition, with a high clay content (Lu et al. 2019; Pang et al. 2021a; Gao et al. 2022). Pores and cracks, as well as clay interstitial minerals, result in a strong microstructure heterogeneity (Siitari-Kauppi et al. 1997; Solano et al. 2017; Ba et al. 2017, 2019; Kumar et al. 2019; Ghasemi et al. 2020; Ma et al. 2021), thus greatly affecting the reservoir response to AE fields (Kozlovskaya and Hjelt 2000; Kazatchenko 2004; Bakar, et al. 2019; Cilli and Chapman 2018; Dutilleul et al. 2020; Leger and Luquot 2021).

Microstructure heterogeneity results in a diversity of petrophysical behaviors (Anguy et al. 1996; Nover 2005; Heise and Ellis 2016; Pang et al. 2019; Mahanta et al 2020; Iqbal et al. 2021; Ozotta et al. 2021; Iwamori et al. 2021; Zhang et al. 2021, 2022; Shen et al. 2022; Wu et al. 2022), including infiltration, acoustic velocity and attenuation, and electrical properties. Sun et al. (2019) built 3D digital cores of tight sandstones with different crack diameters, lengths and dip angles using computed tomography (CT) and studied the effects of the pore geometry on the infiltration characteristics. Fliedner and French (2021) used a differential-equivalent-medium (DEM) model and rock images to quantify the contribution of mineralogy, mineral fabric, porosity and pore shape to the P- and S-wave velocities. Pang et al. (2021a) studied the pore structure and mineralogy of tight-oil rocks by scanning electron microscopy (SEM) and ultrasonic experiments and concluded that the microstructure greatly affects the inelastic properties. More recently, Wang et al. (2022) obtained multi-component digital rocks based on CT scans, maps and SEM multi-scale experiments, estimating the resistivity by a finite-element method and studying the influence of the pore geometry and mineral composition on the electrical properties.

Joint AE properties are generally applied to estimate the characteristics of subsurface rocks (Heinson 1999; Hacikoylu et al. 2006; Carcione et al. 2007; Han et al. 2011, 2020; Jensen et al. 2013; Gomes et al. 2017; Cilli and Chapman 2018; Attias et al. 2020; Amalokwu and Falcon-Suarez 2021). Many experimental and theoretical works estimate the effect of pore structure and mineralogy on the AE properties of rocks (Gabas et al. 2016; Falcon-Suarez et al. 2019; Cilli and Chapman 2020). Gomez et al. (2010) experimentally established relations among resistivity, elastic velocity, porosity and permeability of sandstones and used the self-consistent approximation to simulate the AE properties of rocks. Pride et al. (2017) studied changes in geophysical properties caused by fluid injection, specifically seismic velocity and conductivity of sandstone and granite samples. Wu et al. (2020) proposed a hybrid stochastic (HS) algorithm, combined the quartet structure generation set and discrete finite-element method to establish multi-scale and multi-composition digital models and simulated

the rock resistivity and elastic moduli. Pang et al. (2021b) established a 3D rock physics model (RPM) to simulate the effect of mineral composition, pore structure and fluid saturation on AE properties and calibrated the model with well-log data.

In order to characterize the rock microstructure, we extract cores from a tight-oil reservoir of Yanchang Formation in the *Q* Area, Ordos Basin, China. Then, X-ray diffraction (XRD), casting thin sections (CTS), ultrasonic wave and electrical resistivity experiments under different confining pressures are performed. The pore structure and mineralogy of the rocks is analyzed, and the relation between the AE properties and porosity, pressure (crack) and mineral composition is studied. Based on the mineral composition and thin section analysis, we use a triple-porosity model to describe the acoustic properties of the rock (Sun et al. 2016; Ma et al. 2019).

In the acoustic RPM, the Hashin–Shtrikman equation (Hashin and Shtrikman 1963) is used to estimate the elastic modulus of the mineral mixture, and the acoustic DEM (A-DEM) equation (Berryman 1992) to add clay minerals, pores and cracks into the minerals. The final (saturation) model is obtained with the triple-porosity equation. We implement the electrical HS (E-HS) (Hashin and Shtrikman 1962), DEM (E-DEM) (Cilli and Chapman 2021) equations and Cole–Cole model (Cole and Cole 1941; Pelton et al. 1978) to estimate the electrical properties of the mineral mixture and rock frame containing the clay minerals, pores and cracks to obtain the electrical RPM. Thus, the AE models with the same microstructure are used to analyze the response to porosity, crack porosity and clay content. A 3D AE rock physics template (RPT) is built with the elastic attributes and resistivity and calibrated with core and well-log data and applied to the tight-oil reservoirs.

2 Geological Characteristics and Rock Microstructure

The prospect is located in the *Q* area of Ordos Basin, which has a complex tectonic history and warm and humid climate, resulting in the deposition of hydrocarbon source rocks rich in organic matter (Liu et al. 2021). The burial depth of Member 7 of the Yanchang Formation is located between 1200 and 2350 m. The sediments of the tight-oil reservoirs in this formation are mainly lacustrine facies with high-quality source rocks widely distributed. The reservoir lithology is mainly tight sandstone intercalated with mudstone and mud shale intercalated with thin sandstone. The sandstone layer is the main section of the reservoir in Member 7, which is characterized by developed microcracks and micro-/nanopore throats. The pore radius is mainly 2–8 μm. The pore structure favors the reservoir capacity and contributes to the hydrocarbon accumulation (Fan et al. 2021; Ji et al. 2022).

We select 9 core samples (A–I) from the reservoirs to perform the CTS and XRD experiments. Figure 1 shows the thin sections of sample I. The reservoir space is mainly dominated by intergranular and dissolved pores and microcracks. The interstitial materials in the rocks are mainly clay and a small amount of cement such as carbonate and siliceous minerals. The existence of pores, cracks and fillings results in strong heterogeneity of the microstructure. Figure 2 shows the mineral compositions of the samples. The minerals are mainly quartz, feldspar, carbonate minerals, clay and a small amount of ore mineral. The quartz content is high, and feldspar is mainly

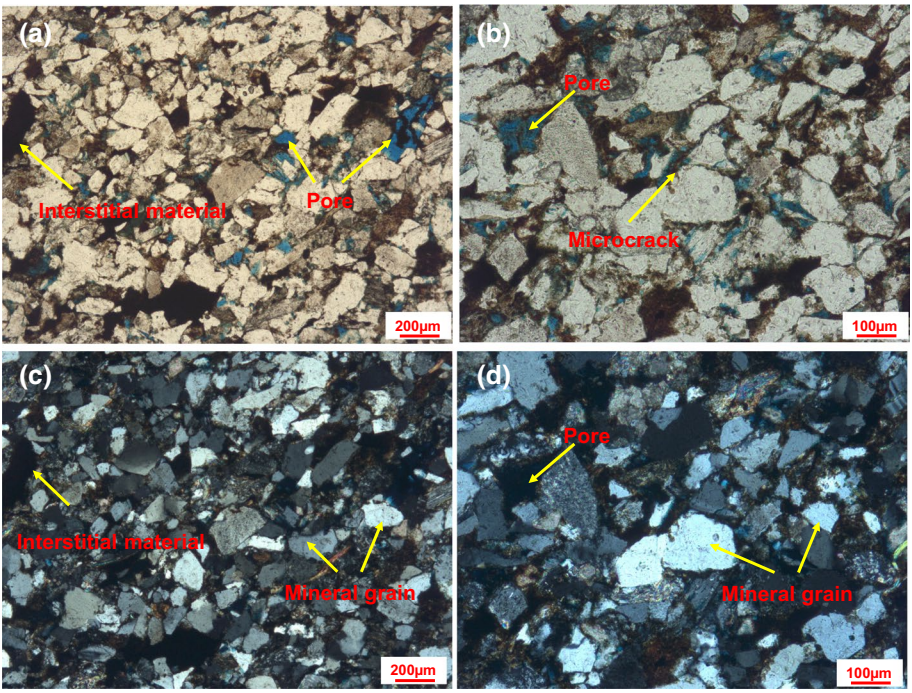

Fig. 1 Thin sections of the tight-oil rock sample I, showing the intergranular and dissolved pores, microcracks and interstitial materials. Figure 1a, b shows thin section I in plane polarized light (PPL), and 1c and 1d in cross-polarized light (XPL), respectively

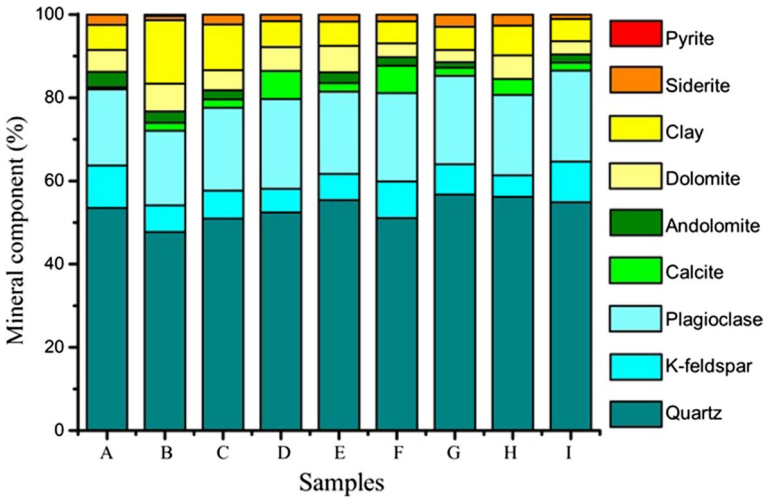

Fig. 2 Mineral components of the rock samples. Please note that pyrite occurs only in Sample B with 0.35%

Table 1 Properties of the samples

Sample	A	B	C	D	E	F	G	H	I
Depth (m)	2036.5	2000.6	1948.2	1819.5	2341.5	1979.6	1964	2101.83	1996
Porosity (%)	3.56	4.49	5.28	6.38	7.33	7.79	8.85	9.20	10.16
Permeability (mD)	0.005	0.033	0.005	0.018	0.019	0.042	0.065	0.038	0.096
Clay content (%)	6.03	15.23	10.96	6.23	5.85	5.29	5.55	7.12	5.35
Dry-rock density (g/cm^3)	2.58	2.57	2.53	2.49	2.48	2.44	2.41	2.44	2.37

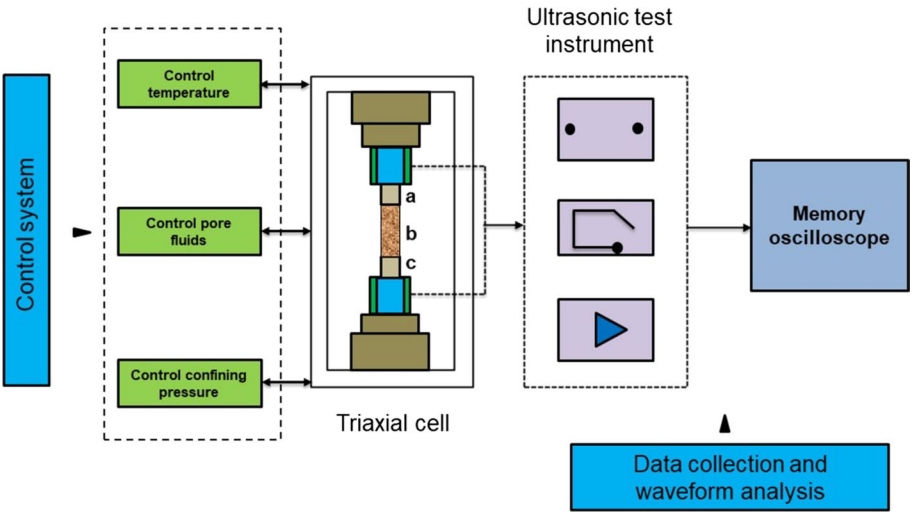

Fig. 3 Ultrasonic equipment. **a** Transmitter; **b** Specimen; and **c** Receiver

plagioclase and potassium feldspar, where the plagioclase content is higher. The clay minerals are mainly laumontite and chlorite, and ore minerals are siderite and pyrite.

3 Acoustic and Electrical Properties of the Tight-Oil Rocks

3.1 Laboratory Experiments

Nine samples with different porosity and clay content are used to perform the ultrasonic and electrical experiments. The contribution of microcracks (soft pores) cannot be ignored. Experiments and theories have proved that microcracks are highly affected by effective pressure (David and Zimmerman 2012; Zhang et al. 2019). Thus, ultrasonic-wave and resistivity measurements are performed to analyze the influence of cracks on the AE properties by applying different confining pressures. Cylindrical rock specimens with a diameter of 25.077–25.147 mm and a length of 48.803–50.093 mm are extracted from the initial rock samples (see Table 1).

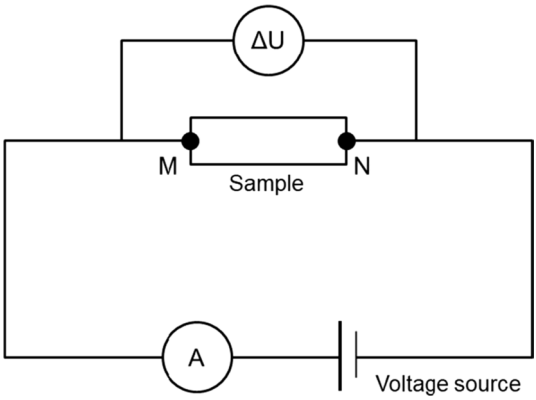

Fig. 4 Schematic diagram of the resistivity measurement principle, A is electric current, ΔU is voltage (potential difference), and M and N are electrodes

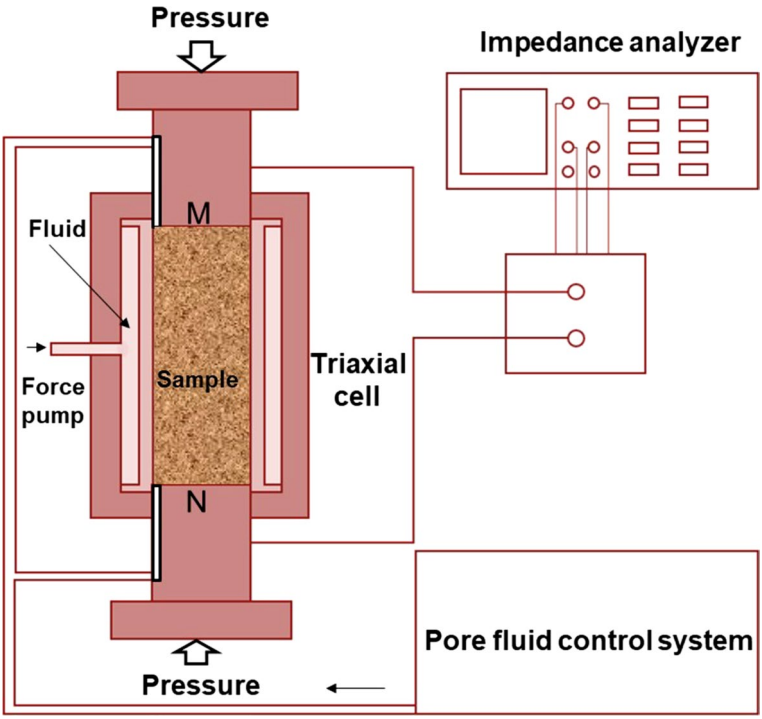

Fig. 5 Experimental apparatus to measure rock resistivity. M and N denote electrodes

Firstly, the ultrasonic experiments are carried out. The equipment (Fig. 3) is used to measure the elastic velocities by the pulse method at 25 °C and a pore pressure of 15 MPa within ultrasonic frequency range (MHz). The samples are saturated with water and then sealed with a rubber sleeve and placed in the equipment. Confining pressures of 20, 30, 40,

50 and 60 MPa are applied to the specimens, and the waveforms are recorded. The elastic velocities are calculated from the first arrivals.

Then, based on the two-electrode method (Fig. 4) and resistivity experimental apparatus shown in Fig. 5, the electrical resistivity is measured with an alternating current at 120 Hz and a voltage of 1 V. The samples are saturated with brine (the salinity is 56.5 g/L). The above confining pressures are applied to the specimens to measure the resistivity ρ (reciprocal of electrical conductivity) which can be computed as

$$\rho = \frac{RS}{L} \tag{1}$$

where R is the resistance, S is the cross-sectional area and L is the sample length.

3.2 Experimental Results

The effects of the microstructures on the AE properties of tight rocks are analyzed based on the experiments. Figure 6a, b shows the ultrasonic P- and S-wave velocities of the samples as a function of the effective pressure (confining minus pore). The velocities increase with pressure. This is due to the microcracks gradually closing, increasing the elastic moduli and velocity of the skeleton. Due to the same reason, the resistivity increases and the

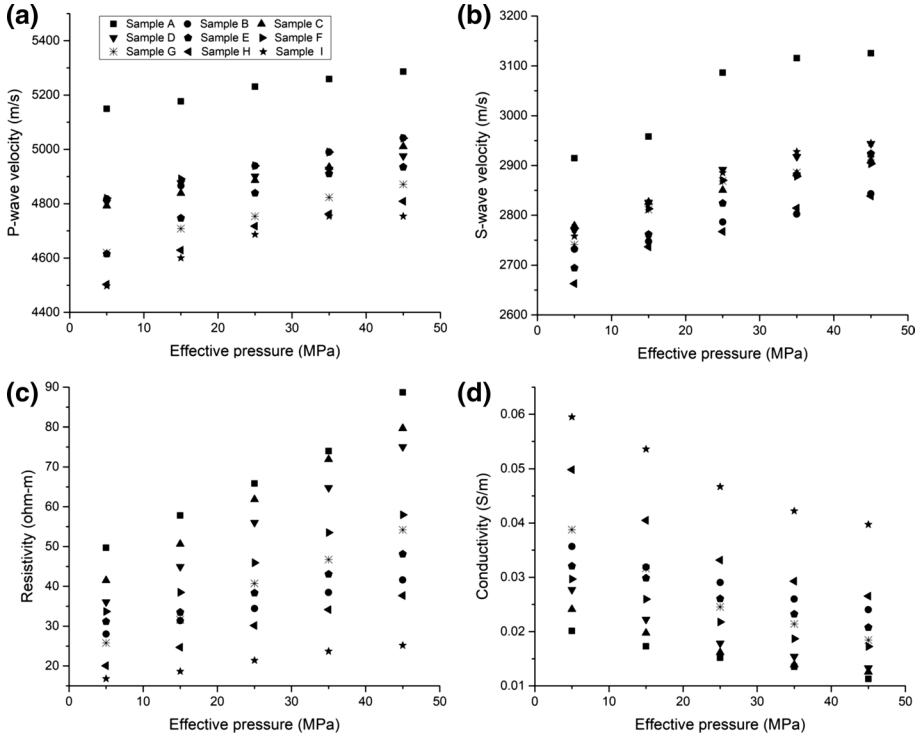

Fig. 6 Ultrasonic P- and S-wave velocities **a**, **b**, resistivity **c** and conductivity **d** as a function of the effective pressure

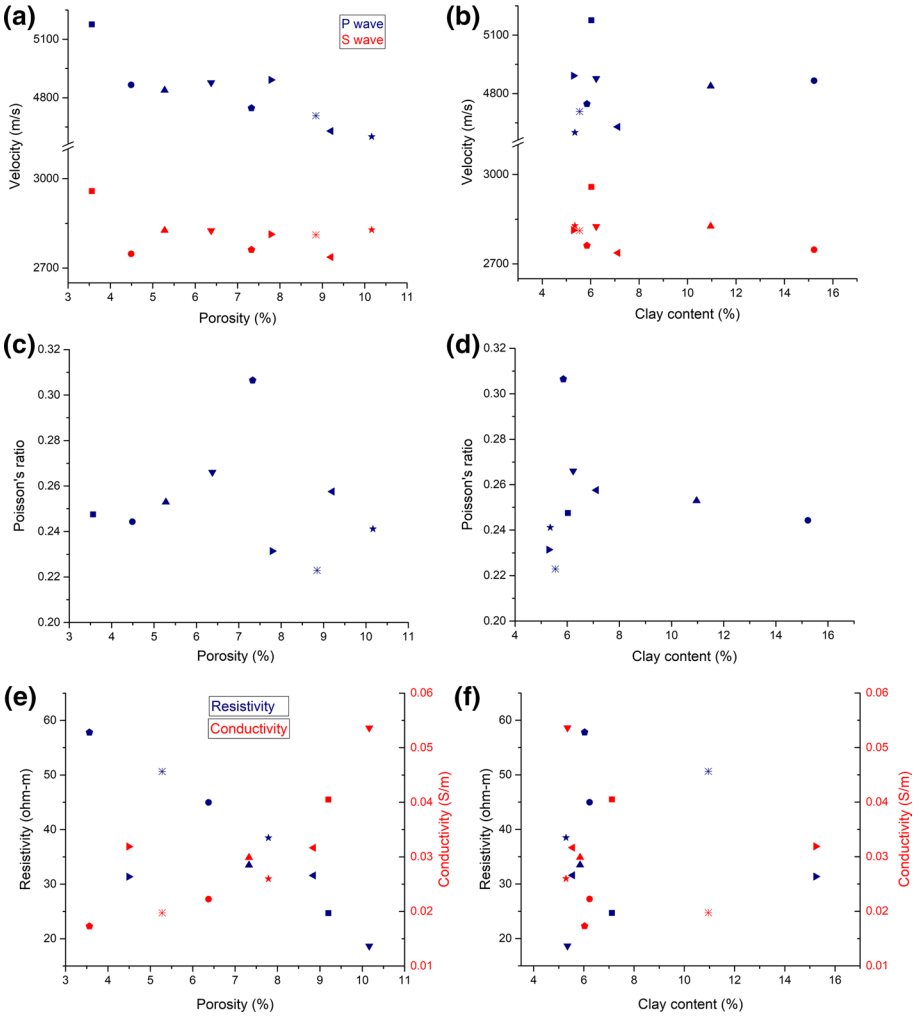

Fig. 7 Ultrasonic P- and S-wave velocities (blue and red) **a**, **b**, Poisson's ratio **c**, **d** and electrical resistivity and conductivity (blue and red) **e**, **f** of the samples with an effective pressure of 15 MPa as a function of porosity and clay content. The symbols are corresponding to Fig. 6

conductivity decreases (Fig. 6c, d). The results show that the crack density greatly affects the AE properties.

In the reservoir, the pore and effective pressures are both about 15 MPa. Then, we select the experimental data of 30 MPa confining pressure to analyze the AE properties with porosity and clay content under in-situ conditions. Figure 7 shows the P- and S-wave velocities, Poisson's ratio, resistivity and conductivity as functions of porosity and clay content at an effective pressure of 15 MPa, respectively. The elastic attributes (velocities and Poisson's ratio) have no clear relations with porosity due to the influence of the clay minerals. However, there is a relatively good correlation between the electrical properties and porosity. The resistivity of the samples basically decreases with increasing porosity, and the conductivity increases as expected. In Fig. 7b, d and f, there is no evident trend between the

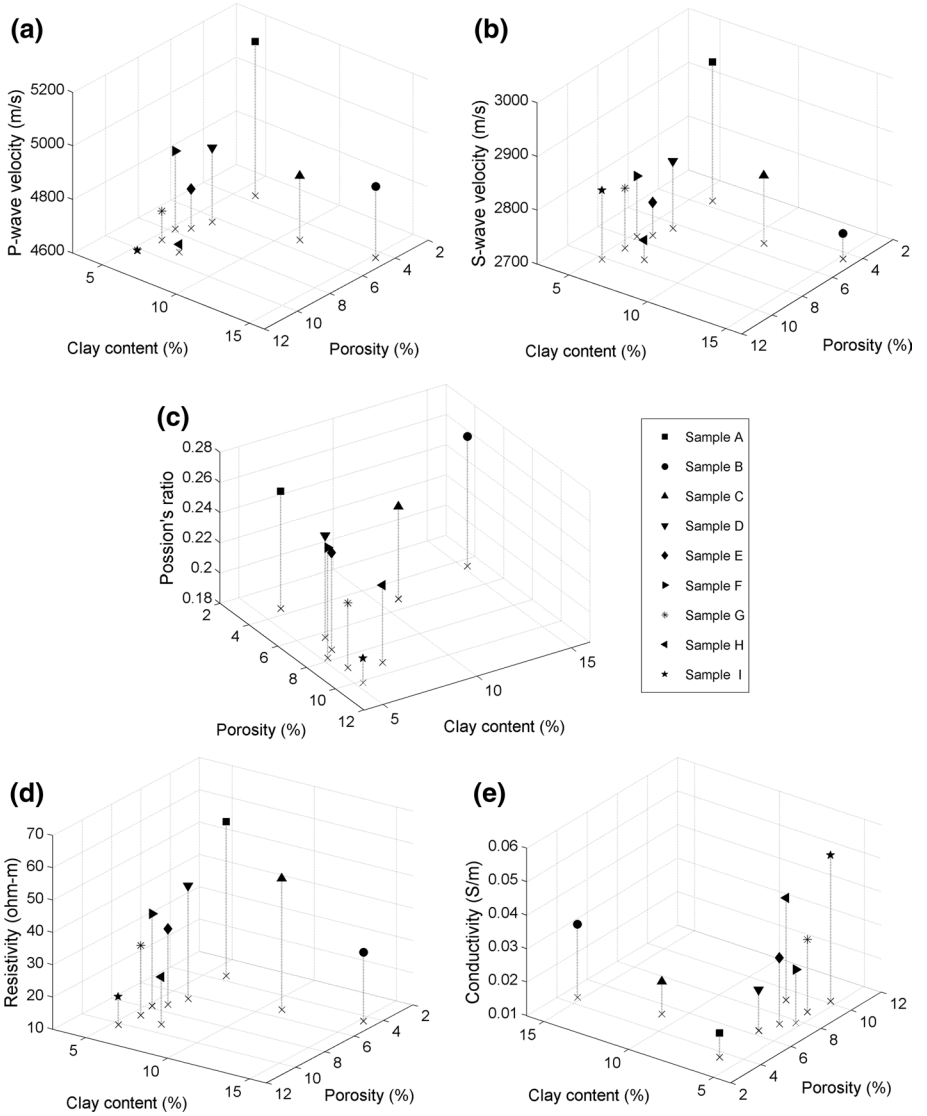

Fig. 8 Ultrasonic P- and S-wave velocities **a**, **b**, Poisson's ratio **c**, resistivity **d** and conductivity **e** as a function of porosity and clay content

elasticity and electrical behaviors and the clay content. It can be inferred that the AE properties are affected by the combination of pore structure and clay minerals.

We use 3D schematic diagrams to analyze the behavior of the AE properties with porosity and clay content, as shown in Fig. 8, where the colors represent different samples. The velocities decrease with porosity and clay content (Fig. 8a, 8b). Sample A shows the highest velocity due to its low porosity and clay content. Samples B and C have also have low porosity, but low velocity because of the high clay content. The other samples have similar clay content and the velocities are well correlated with porosity.

Poisson's ratio shows a poor correlation with both porosity and clay content (Fig. 7c, 7d); however, the trend is better in Fig. 8c. Poisson's ratio decreases with porosity and increases with clay content when the effect of one of them is removed. This is why the Poisson's ratio of the sample I with high porosity and low clay content is the lowest. In Fig. 8d, 8e, samples A and D to I with similar clay content show that the electrical properties are well correlated with porosity. As porosity increases, resistivity decreases and conductivity increases. Similarly, the behavior of samples A, B and C, with similar porosity, indicates that the resistivity decreases with clay content, which explains the divergences between the electrical attributes and porosity of sample B in Fig. 7e due to its high clay content.

4 Rock Physics Models (RPM)

Figure 9a shows a thin section of a tight-oil core, with intergranular pores, microcracks and interstitial fillings containing laumontite and chlorite, which results in strong heterogeneities. The rock microstructure can be modeled by three isotropic frames, associated

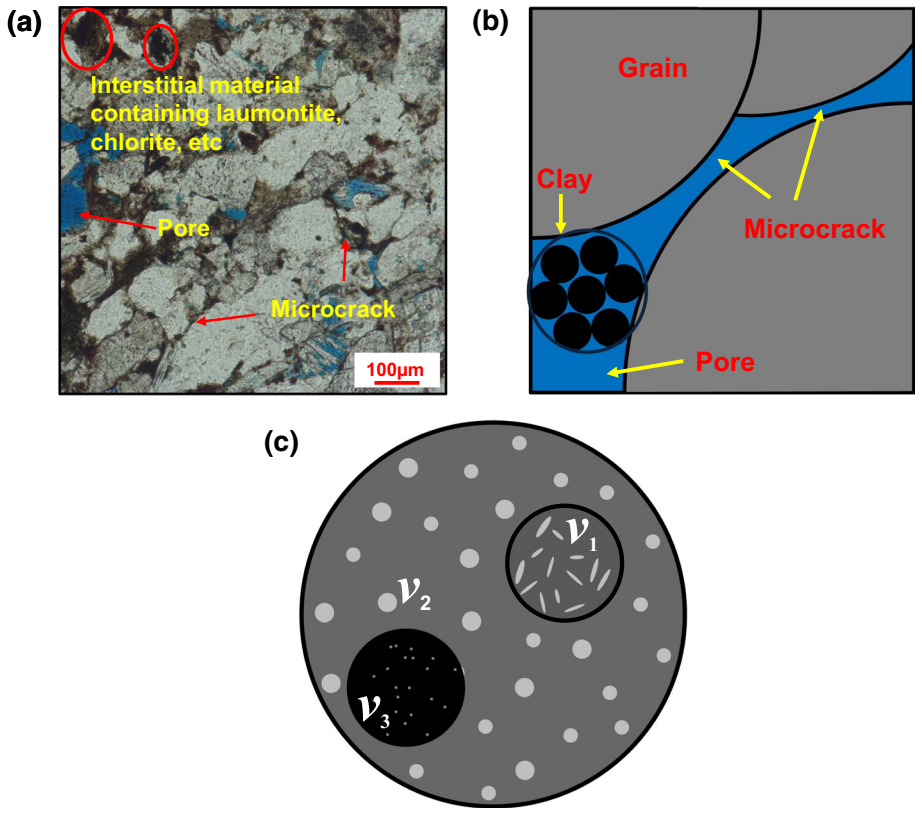

Fig. 9 Tight-oil rock: **a** thin section, **b** schematic diagram of the microstructure and **c** triple-porosity model (v_1, v_2 and v_3 are the volume content of the crack inclusion, host and clay inclusion, respectively)

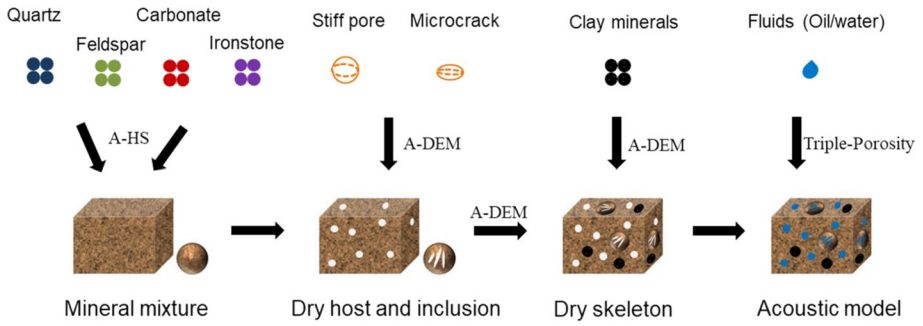

Fig. 10 Modeling flowchart of the acoustic RPM

with pores, cracks and clay minerals (Fig. 9b). Thus, we consider a triple-porosity structure (Fig. 9c) to build the AE RPMs of the tight-oil rock.

4.1 Acoustic RPM

Figure 10 shows the modeling sequence of the acoustic RPM. Firstly, on the basis of XRD experiments, the rock minerals are mainly composed of quartz, feldspar, clay, calcite, dolomite and a small amount of ore mineral. The A-HS (Hashin and Shtrikman 1963) equation is used to calculate the bulk and shear moduli of the mineral mixture (excluding the clay minerals). Berryman (1995) proposed a more general form of the bounds for more than two phases (Mavko et al. 2009),

$$\begin{aligned} K^{\mathrm{HS}+} &= \Lambda\left(\mu_{\max}\right) & K^{\mathrm{HS}-} &= \Lambda\left(\mu_{\min}\right), \\ \mu^{\mathrm{HS}+} &= \Gamma\left(\zeta\left(K_{\max},\mu_{\max}\right)\right), & \mu^{\mathrm{HS}-} &= \Gamma\left(\zeta\left(K_{\min},\mu_{\min}\right)\right), \end{aligned} \tag{2a}$$

$$\Lambda(z) = \left(\sum_{i=1}^{\mathrm{N}} \frac{f_i}{K_i + \frac{4}{3}z}\right)^{-1} - \frac{4}{3}z, \tag{2b}$$

$$\Gamma(z) = \left(\sum_{i=1}^{\mathrm{N}} \frac{f_i}{\mu_i + z}\right)^{-1} - z, \tag{2c}$$

$$\zeta(K,\mu) = \frac{\mu}{6}\left(\frac{9K + 8\mu}{K + 2\mu}\right), \tag{2d}$$

where K_i and μ_i are the bulk and shear modulus of the single phases and f_i is the corresponding volume fraction.

Stiff pores and cracks are added into the host mineral and inclusion, with aspect ratios of 1 and 0.001, respectively, by using the A-DEM equation (Berryman 1992). Then, clay inclusions (with few pores), whose aspect ratio is 1, are added into the host frame by using the A-DEM equation to obtain the dry-rock moduli, K^* and μ^*,

$$(1-y)\frac{\mathrm{d}}{\mathrm{d}y}\left[K^*(y)\right] = \left(K_2 - K^*\right)P^{(*2)}(y), \tag{3a}$$

$$(1-y)\frac{\mathrm{d}}{\mathrm{d}y}\left[\mu^*(y)\right] = \left(\mu_2 - \mu^*\right)Q^{(*2)}(y), \tag{3b}$$

With $K^*(0)=K_1$, $G^*(0)=G_1$, where K_1 and G_1 are the bulk and shear moduli of the host phase, and K_2 and G_2 those of phase 2, y is the corresponding content, and P^{*i} and Q^{*i} represent the geometrical factors of the ith component (see Appendix 1).

The bulk modulus and density of the fluids at reservoir conditions are estimated as in Batzle and Wang (1992). Finally, the triple-porosity equation (see Zhang et al. 2017) is used to obtain the wet-rock properties (all the pores are filled with fluids),

$$\begin{aligned} &N\nabla^2\mathbf{u} + (A+N)\nabla e + Q_1\nabla\left(\xi_1+\phi_2\zeta_{12}\right) + Q_2\nabla\left(\xi_2-\phi_1\zeta_{12}+\phi_3\zeta_{23}\right) + Q_3\nabla\left(\xi_3-\phi_2\zeta_{23}\right) \\ &\quad = \rho_{00}\ddot{\mathbf{u}} + \rho_{01}\ddot{\mathbf{U}}^{(1)} + \rho_{02}\ddot{\mathbf{U}}^{(2)} + \rho_{03}\ddot{\mathbf{U}}^{(3)} + b_1\left(\dot{\mathbf{u}}-\dot{\mathbf{U}}^{(1)}\right) + b_2\left(\dot{\mathbf{u}}-\dot{\mathbf{U}}^{(2)}\right) + b_3\left(\dot{\mathbf{u}}-\dot{\mathbf{U}}^{(3)}\right), \end{aligned} \tag{4a}$$

$$Q_1\nabla e + R_1\nabla\left(\xi_1+\phi_2\zeta_{12}\right) = \rho_{01}\ddot{\mathbf{u}} + \rho_{11}\ddot{\mathbf{U}}^{(1)} - b_1\left(\dot{\mathbf{u}}-\dot{\mathbf{U}}^{(1)}\right), \tag{4b}$$

$$Q_2\nabla e + R_2\nabla\left(\xi_2-\phi_1\zeta_{12}+\phi_3\zeta_{23}\right) = \rho_{02}\ddot{\mathbf{u}} + \rho_{22}\ddot{\mathbf{U}}^{(2)} - b_2\left(\dot{\mathbf{u}}-\dot{\mathbf{U}}^{(\mathbf{2})}\right), \tag{4c}$$

$$Q_3\nabla e + R_3\nabla\left(\xi_3-\phi_2\zeta_{23}\right) = \rho_{03}\ddot{\mathbf{u}} + \rho_{33}\ddot{\mathbf{U}}^{(3)} - b_3\left(\dot{\mathbf{u}}-\dot{\mathbf{U}}^{(3)}\right), \tag{4d}$$

$$\begin{aligned} &\frac{1}{3}\rho_f R_{12}^2\ddot{\zeta}_{12}\phi_2^2\phi_1\left(\frac{1}{5}+\frac{\phi_{10}}{\phi_{20}}\right) + \frac{1}{3}\left(\frac{\eta}{5\kappa_1}+\frac{\eta}{\kappa_2}\right)R_{12}^2\dot{\zeta}_{12}\phi_2^2\phi_1\phi_{10} \\ &\quad = \phi_2\left(Q_1 e + R_1\left(\xi_1+\phi_2\zeta_{12}\right)\right) - \phi_1\left(Q_2 e + R_2\left(\xi_2-\phi_1\zeta_{12}+\phi_3\zeta_{23}\right)\right), \end{aligned} \tag{4e}$$

$$\begin{aligned} &\frac{1}{3}\rho_f R_{23}^2\ddot{\zeta}_{23}\phi_2^2\phi_3\left(\frac{1}{5}+\frac{\phi_{30}}{\phi_{20}}\right) + \frac{1}{3}\left(\frac{\eta}{5\kappa_3}+\frac{\eta}{\kappa_2}\right)R_{23}^2\dot{\zeta}_{23}\phi_2^2\phi_3\phi_{30} \\ &\quad = \phi_3\left(Q_2 e + R_2\left(\xi_2-\phi_1\zeta_{12}+\phi_3\zeta_{23}\right)\right) - \phi_2\left(Q_3 e + R_3\left(\xi_3-\phi_2\zeta_{23}\right)\right), \end{aligned} \tag{4f}$$

where $\mathbf{u}$ denotes the solid displacement vector, $\dot{\mathbf{U}}^{(1)}$, $\dot{\mathbf{U}}^{(2)}$ and $\dot{\mathbf{U}}^{(3)}$ are the displacement vectors of the fluids in cracks, pores and clay micropores, respectively, e, ξ_1, ξ_2 and ξ_3 are the corresponding divergences, and ζ_{12} and ζ_{23} are the variations in fluid content owing to the local fluid flow between cracks and intergranular pores and between clay and intergranular pores, respectively. The quantities κ_1, κ_2 and κ_3 are the permeabilities of the crack, host and clay-mineral frames, respectively, R_{12} and R_{23} are the radii of the crack and clay inclusions, respectively. The volume ratio and porosity of the crack are v_1 and ϕ_{10}, while those of the host skeleton are v_2 and ϕ_{20}, and those of the clay inclusion are v_3 and ϕ_{30}, respectively; $v_1+v_2+v_3=1$, and ϕ_1, ϕ_2 and ϕ_3 are the absolute porosities of the crack, host and clay skeletons, respectively, and $\phi_1+\phi_2+\phi_3$ is the total porosity, and $\phi_1=v_1\phi_{10}$, $\phi_2=v_2\phi_{20}$ and $\phi_3=v_3\phi_{30}$; ρ_f and η denote the fluid density and viscosity, respectively. The stiffness coefficients A, N, Q_1, Q_2, Q_3, R_1, R_2 and R_3, dissipation coefficients b_1, b_2 and b_3, and density parameters ρ_{00}, ρ_{01}, ρ_{02}, ρ_{03}, ρ_{11}, ρ_{22} and ρ_{33} depend on the rock properties (Appendix 2).

The complex wave number k is estimated from a plane-wave analysis (see Appendix 2), and the wave velocity and quality factor are

$$V_P = \frac{1}{\mathrm{Re}\left(v^{-1}\right)}, \tag{5a}$$

$$Q = \frac{\mathrm{Re}\left(v^2\right)}{\mathrm{Im}\left(v^2\right)}, \tag{5b}$$

where $v = \omega/k$ and ω is the angular frequency (Carcione 2014).

4.2 Results of the Acoustic RPM

The model allows us to analyze the wave response of rock pore structure and mineralogy. The model properties are given in Table 2. The minerals of the crack inclusions and host are same, so the elastic properties of the two phases $K_{s1}=K_{s2}=K_s$, $\mu_{s1}=\mu_{s2}=\mu_s$ and $\rho_{s1}=\rho_{s1}=\rho_s$. Then the skeleton moduli of the three phases (K_{b1} and μ_{b1}, K_{b2} and μ_{b2}, K_{b3} and μ_{b3}) are estimated by the A-DEM equation and then the moduli of the dry rock (K_b and μ_b). The model is set as full-oil saturation. By adjusting the total and crack porosities and clay content, the wave velocity and quality factor can be obtained.

Figure 11 shows the P-wave velocity and dissipation factor at four total porosities (ϕ), crack porosities (ϕ_C) and clay content (V_{sh}) settings, respectively, given in the figure. Figure 11a, b shows two dispersion steps and attenuation peaks, and in Fig. 11c, d, the steps and peaks shift to higher frequencies. Increasing the total and soft porosities and clay content decreases the velocity and increases the attenuation, the latter depending on the frequency band.

4.3 Electrical RPM

Figure 12 shows the modeling workflow of the electrical RPM. Similarly, based on XRD results of the samples, the E-HS (Hashin and Shtrikman 1962) equation is used to calculate the electrical conductivity of the mineral mixture by mixing quartz, feldspar, carbonate and ironstone minerals. Berryman (1995) proposed a more general form of the bounds for more than two phases,

Table 2 Medium properties

Mineral bulk modulus (K_S)	55 GPa	Crack inclusion radius (R_{12})	50 μm
Shear modulus (μ_S)	45 GPa	Porosity (ϕ_{10})	0.01
Density (ρ_S)	2.65 g/cm^3	Aspect ratio	1
Clay bulk modulus (K_{sh})	10.5 GPa	Clay inclusion radius (R_{23})	50 μm
Shear modulus (μ_{Sh})	3.5 GPa	Porosity (ϕ_{30})	0.00001
Density (ρ_{sh})	2.45 g/cm^3	Aspect ratio	1
Water bulk modulus (K_W)	2.24 g/cm$_3$	Pore aspect ratio	1
Viscosity (η_w)	0.00098 Pa s	Crack aspect ratio	0.001
Density (ρ_W)	1.002 GPa		
Oil bulk modulus (K_O)	1.27 Pa s		
Viscosity (η_O)	0.0021 Pa s		
Density (ρ_O)	0.79 g/cm^3		

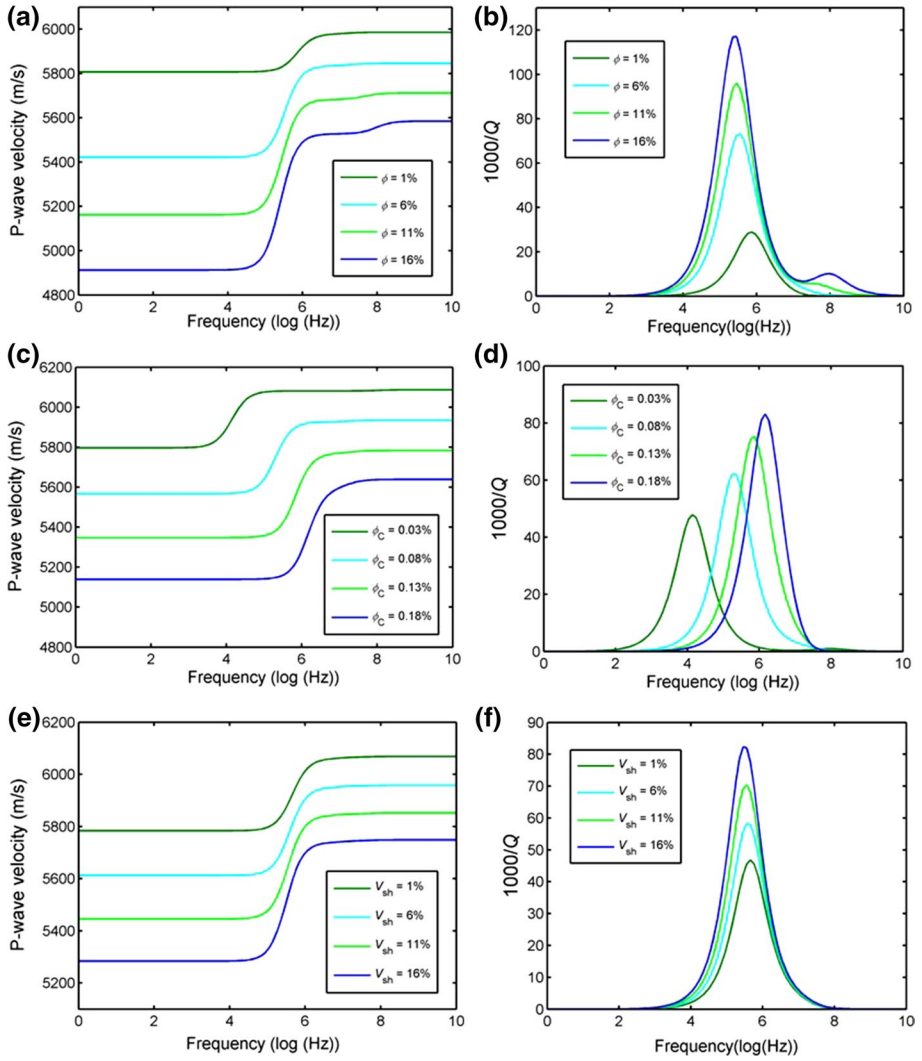

Fig. 11 Wave velocity and dissipation factor of the P wave as a function of frequency at different porosities **a** and **b** ($\phi_C = 0.1\%$ and $V_{sh} = 10\%$), crack porosities **c** and **d** ($\phi = 5\%$ and $V_{sh} = 10\%$), and clay content **e** and **f** ($\phi = 5\%$ and $V_{sh} = 0.1\%$)

$$\sigma^{HS+} = F\left(\sigma_{max}\right)\ \sigma^{HS-} = F\left(\sigma_{min}\right), \tag{6a}$$

$$F(z) = \left(\sum_{i=1}^{N} \frac{f_i}{\sigma_i + 2z}\right)^{-1} - 2z, \tag{6b}$$

where σ^{HS+} and σ^{HS-} are the upper and lower bounds, respectively, σ_i is the conductivity of the single phases and f_i is the volume fraction, and σ_{max} and σ_{min} are the maximum and minimum values.

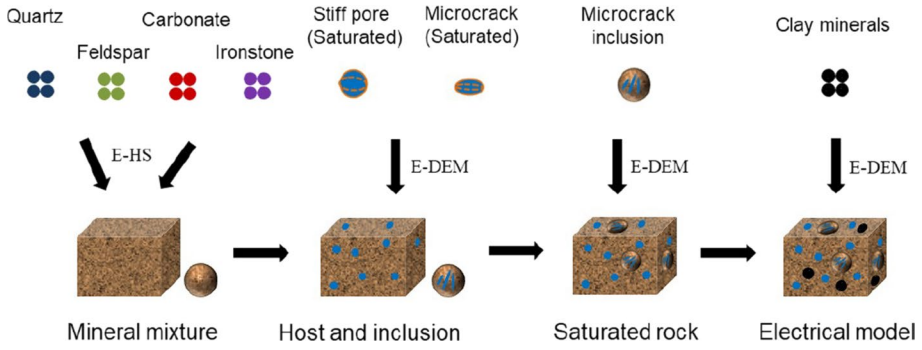

Fig. 12 Modeling flowchart of the electrical RPM

We consider the same microstructure (aspect ratios of pores, cracks) to build the electrical model. The E-DEM equation is used to add pores and cracks containing fluid into the host and inclusions. Then, the crack and clay inclusions are added into the host frame to obtain the conductivity σ^* by using the E-DEM equation, as follows (Cilli and Chapman 2021),

$$(1-y)\frac{\mathrm{d}}{\mathrm{d}y}\left[\sigma^*(y)\right] = \left(\sigma_2 - \sigma^*\right)m, \tag{7}$$

with $\sigma^*(0)=\sigma_1$, where σ_1 is the conductivity of the host phase, σ_2 is the conductivity of phase 2, y is the corresponding content, and m is a function of the depolarizing factor L_P of phase 2:

$$m = \frac{1}{3}\sum_{\mathrm{p}=1}^{3}\left\{\left[1+\left(\frac{\sigma_2}{\sigma^*}-1\right)L_\mathrm{P}\right]\right\}, \tag{8}$$

Archie (1942) assumed a rock without clay and other conductive minerals, so that the rock conductivity only depends on the formation water in the pore space. The additional conductivity of clay minerals is not considered, since the salinity in the target formation is 56.5 g/L (Leveaux and Poupon 1971; Han et al. 2005; Wang et al. 2006). The surface conductivity is also neglected in the studies of tight siltstones (Pang et al. 2021b). Thus, the formation factor and resistivity index are

$$F = \frac{\sigma_\mathrm{W}}{\sigma_\mathrm{r}} = \frac{1}{\phi^\mathrm{M}}, \tag{9a}$$

$$I = \frac{b}{S_\mathrm{w}^n}, \tag{9b}$$

Respectively, where σ_W and σ_r are the water and rock conductivities, respectively, S_W is the saturation, b is a lithology coefficient, and M and n are the parameters (b and n are assumed to be 1 and 2 here, respectively).

According to Archie's equation, the electrical conductivity of pores and cracks as a function of water saturation is,

$$\sigma_2 = b^{-1} S_{\mathrm{W}}^{n} \sigma_{\mathrm{W}}, \tag{10}$$

where σ_2 is the conductivity of pores or cracks.

Finally, the Cole–Cole equation (Cole and Cole 1941; Pelton et al. 1978; Mansoor and Slater 2007) is applied to consider the frequency dependence caused by the polarization effects. The complex conductivity is

$$\sigma^*(\omega) = \sigma_0 \left[1 + \mathrm{mm} \left(\frac{(i\omega\tau)^c}{1 + (i\omega\tau)^c (1 - \mathrm{mm})} \right) \right], \tag{11}$$

where ω is the angular frequency, σ_0 is the conductivity at zero frequency, τ is the relaxation time, mm is the chargeability, and c is a frequency exponent ($0 \le c \le 1$). We have

$$\sigma^*(\omega) = \frac{1}{\mathrm{Rt}^*(\omega)} = \sigma_{\mathrm{real}}(\omega) + i\sigma_{\mathrm{im}}(\omega). \tag{12}$$

where $\mathrm{Rt}^*(\omega)$ is the complex resistivity, $\sigma_{\mathrm{real}}(\omega)$ and $\sigma_{\mathrm{im}}(\omega)$ are the real and imaginary conductivities, respectively, and $i = \sqrt{-1}$.

4.4 Results of the Electrical RPM

Figure 13 shows the effect of frequency, based on the Cole–Cole model, for different values of the parameters. The conductivity and the dispersion effect increase with increasing σ_0 and mm, with σ_0 and mm having low and high impacts (Fig. 13a–d), respectively. The peaks shift to lower frequencies with increasing τ (see Fig. 13e, f). We can see in Fig. 13g, h that the frequency coefficient affects curves. With the increase of c, the dispersion increases and the corresponding frequency band becomes narrow.

We consider the same properties of the acoustic model. The electrical and Cole–Cole models are used to analyze the responses of pores, cracks and clay mineral. The conductivity obtained by the E-DEM model is set as the zero-frequency conductivity σ_0, and mm, τ and c are 0.05, 0.1 and 0.87, respectively (Revil et al. 2018). The conductivities of the clay, brine and mineral mixture are 0.5, 4.69 and 0.01 S/m (Han et al. 2016; Pang et al. 2021b), respectively, and the rock is saturated with water. The results are shown in Fig. 14, where we can see that with the increase of the total and crack porosities and clay content, the conductivity and dispersion increase. It is shown that these are less affected by the rock microstructure.

We consider a frequency of 120 Hz and water saturation from 0 to 1 to analyze the effects of the rock microstructure on conductivity and formation factor. Figure 15 shows the conductivity and formation factor of as a function of the water saturation at five values ϕ, ϕ_{C} and V_{sh} settings, indicated in the figure. The conductivity increases and the formation factor decreases with increasing water saturation. At low saturation, the conductivity decreases with increasing total and crack porosities. However, the electrical properties show an opposite trend when the saturation exceeds a certain value (see Fig. 15a–d). This is because when the water saturation is low, the conductivity of the pores and cracks containing fluids is lower than the mineral mixture, so the rock conductivity decreases with the porosity. With increasing saturation, the conductivity of pores and cracks are higher than that of the minerals, resulting in an increase in the rock conductivity. In Fig. 15e, f, the conductivity increases with clay content, and the formation factor decreases, as expected.

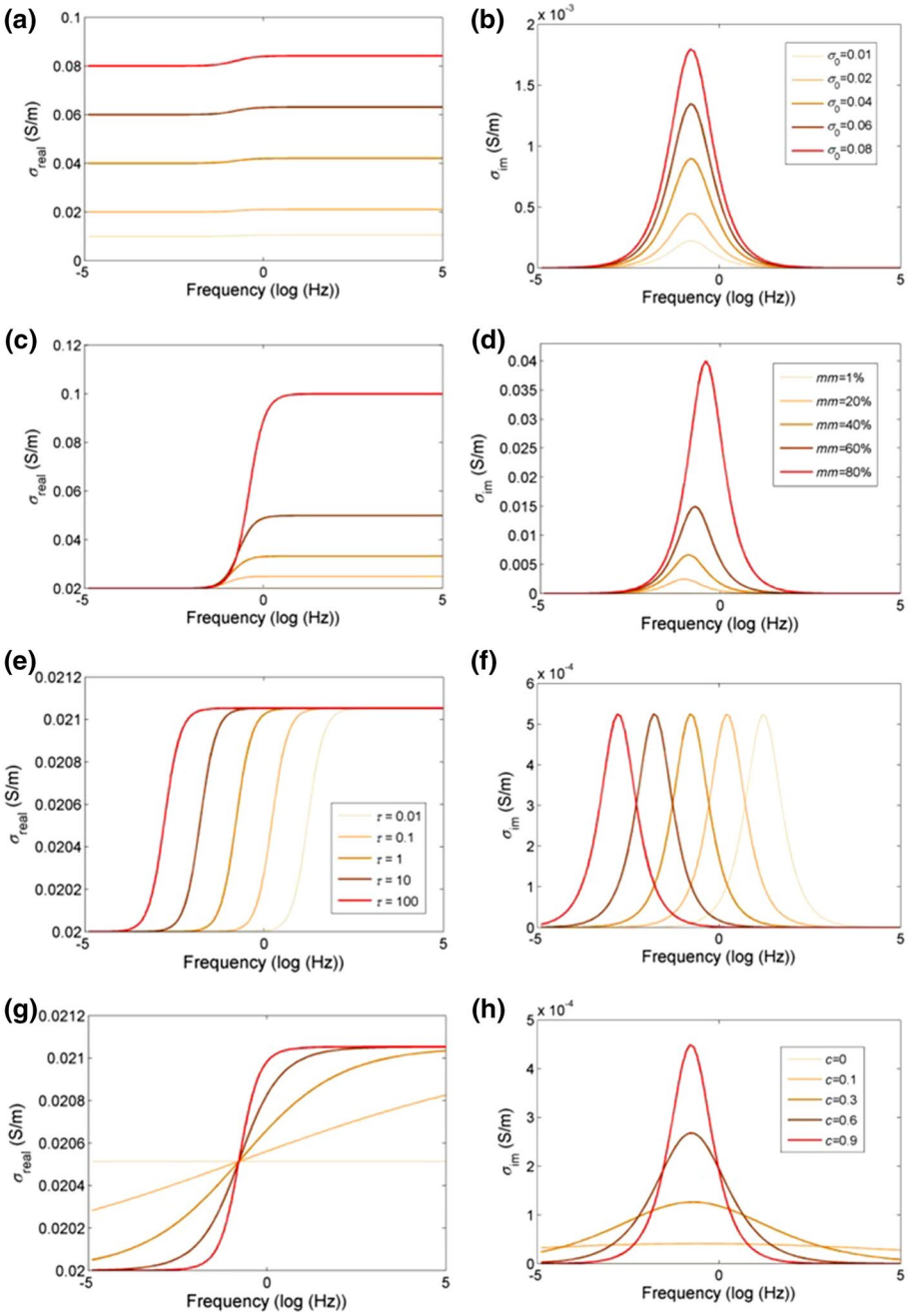

Fig. 13 Real and imaginary conductivities as a function of frequency at different σ_0 (**a** and **b**, mm = 0.05, $\tau = 0.1$ and $c = 0.87$), mm (**c** and **d**, $\sigma_0 = 0.02$, $\tau = 0.1$ and $c = 0.87$), τ (**e** and **f**, $\sigma_0 = 0.02$, mm = 0.05 and $c = 0.87$) and c (**g** and **h**, $\sigma_0 = 0.02$, mm = 0.05, and $\tau = 0.1$)

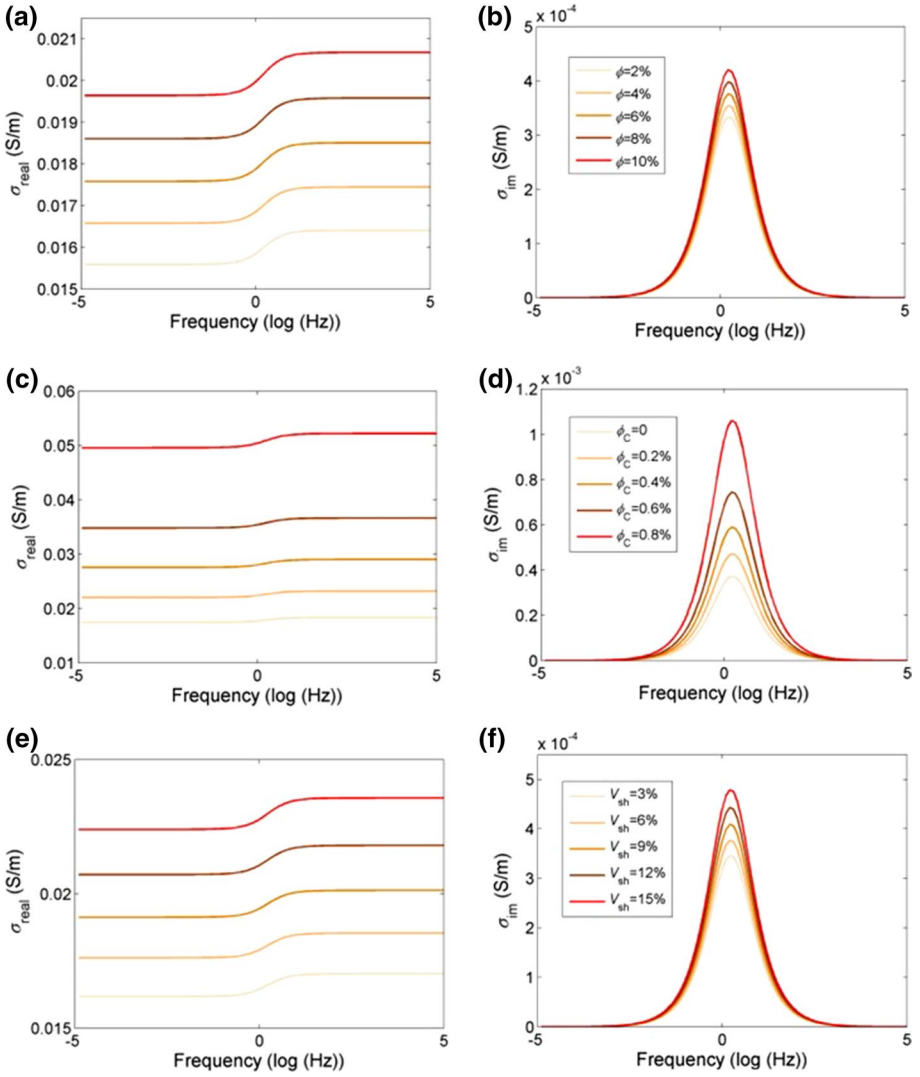

Fig. 14 Real and imaginary conductivities as a function of frequency for different porosities (**a** and **b**), crack porosities (**c** and **d**) and clay contents (**e** and **f**), mm $=0.05$, $\tau=0.1$ and $c=0.87$

5 Rock Physics Template and Application

5.1 3D Rock Physics Template

3D rock physics templates (RPT) can be built by using the elastic attributes (Poisson's ratio (v), and acoustic impedance (AI)) and electrical property (resistivity (R_t)). Figure 16 shows the template and experimental data (symbols), where the color bar corresponds to the effective pressure, and the black, red and blue lines are isolines of total

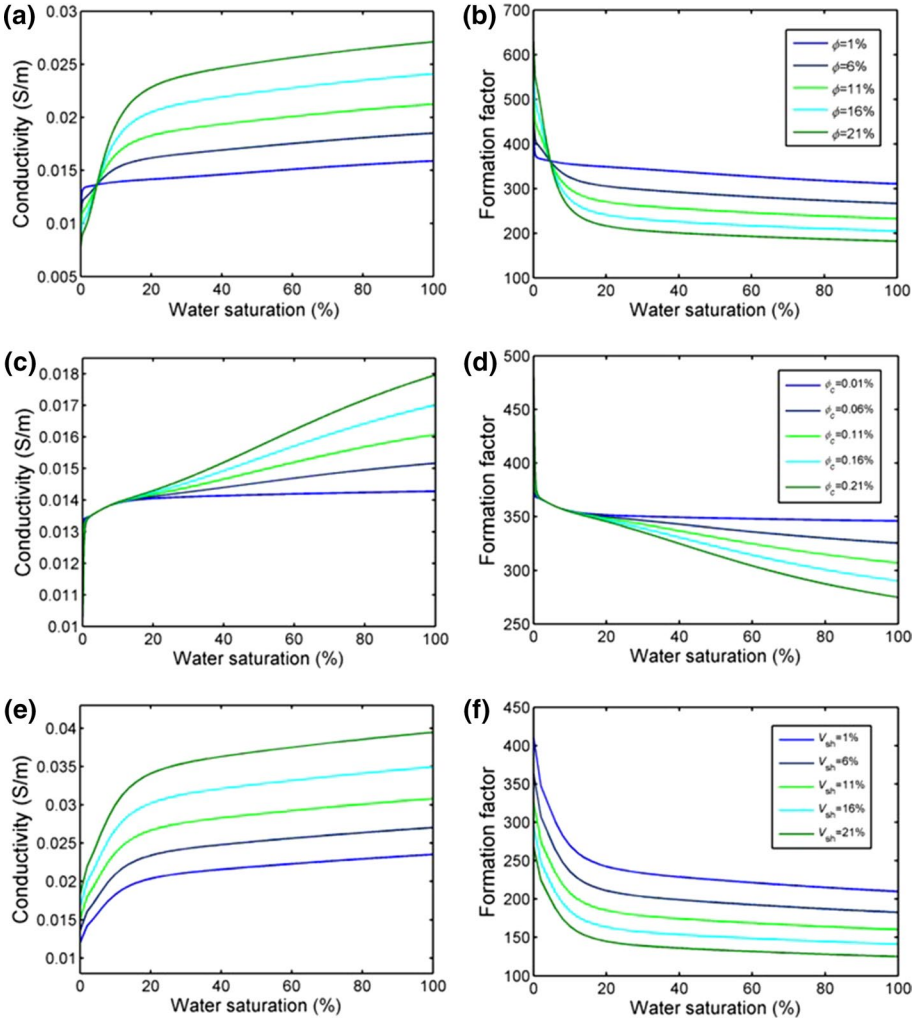

Fig. 15 Resistivity and conductivity as a function of water saturation at different porosities **a** and **b** ($\phi_C = 0.1\%$ and $V_{sh} = 10\%$), crack porosities **c** and **d** ($\phi = 1\%$ and $V_{sh} = 10\%$), and clay content **e** and **f** ($\phi = 10\%$ and $V_{sh} = 0.1\%$)

porosity, crack porosity and clay content, within the range of 3–15%, 0.005–0.625% and 1–19%, respectively. As the pressure decreases, the AE properties agree with the data.

Similarly, data with an effective pressure of 15 MPa (in-situ condition) are selected, as shown in Fig. 17, where the color bar represents porosity and clay content, respectively. The porosity agrees very well, whereas the clay content departs for a small number of samples.

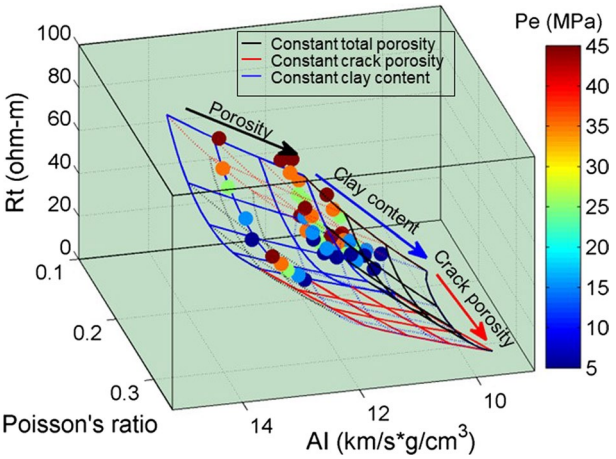

Fig. 16 3D acoustic-electrical RPT and samples, the color is effective pressure

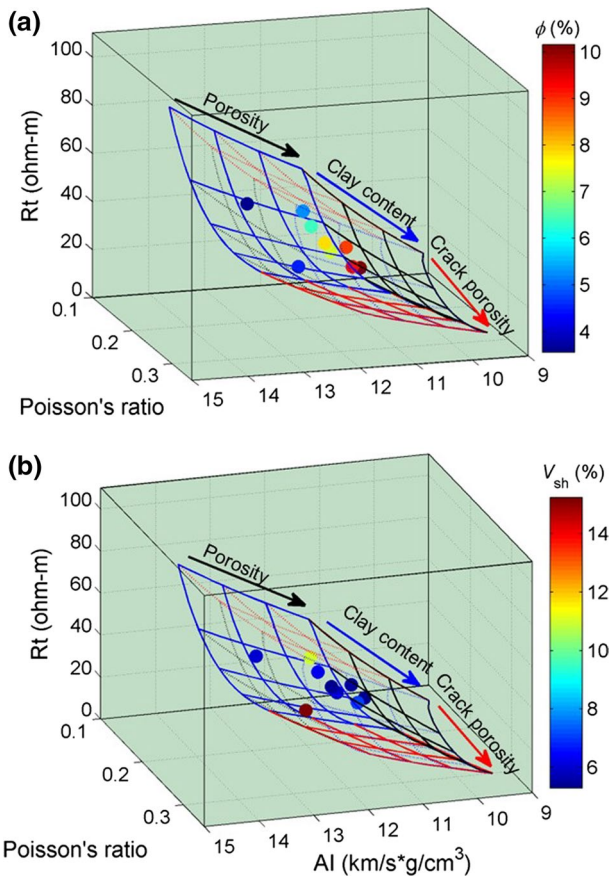

Fig. 17 3D RPT and data (symbols): **a** porosity; **b** clay content

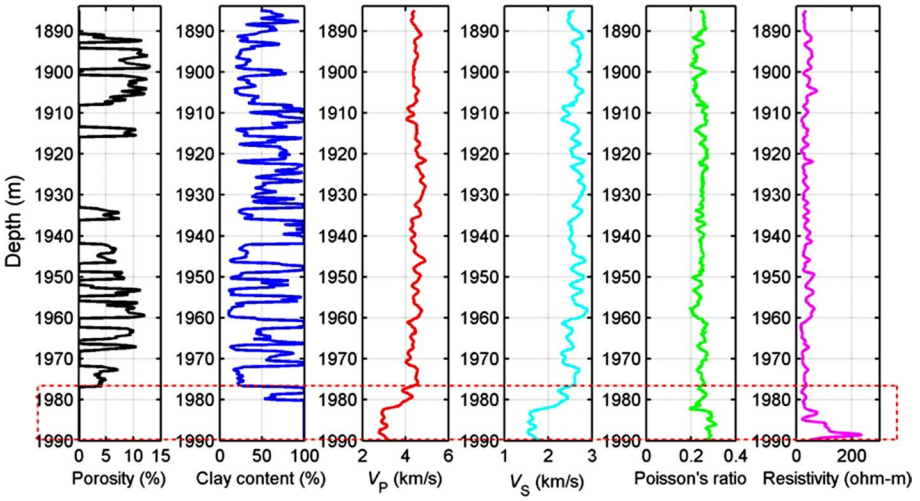

Fig. 18 Petrophysical properties at Well A. The dashed box indicates the mudstone section

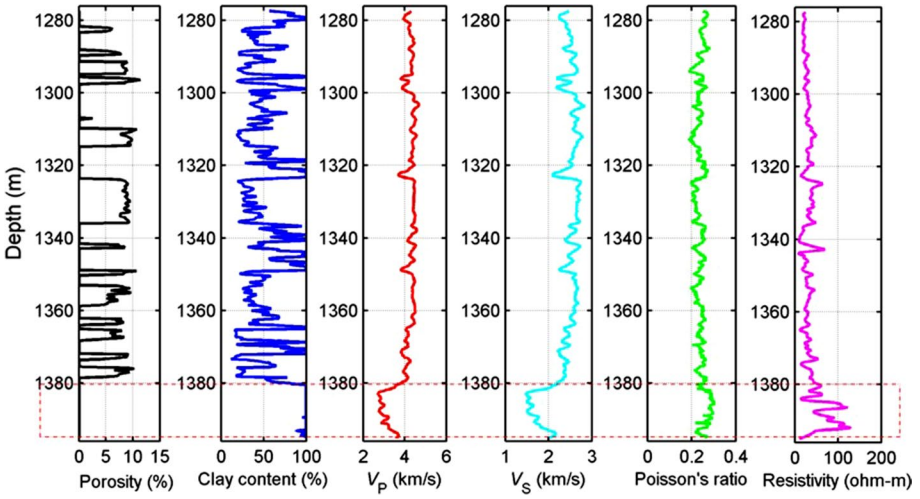

Fig. 19 Same as Fig. 18 but for Well B

5.2 Well Data and Calibration

Well log data of the target reservoir are used to calibrate the RPT. Figures 18 and 19 show the logs at Wells A and B. The reservoir has low porosity (less than 13%) and a wide range of clay content, being a mixture of sandstone, muddy sandstone and mudstone layers. There is a large difference in petrophysical behaviors between the different formations (the dotted box is the mudstone layer). The sandstone layer is the main

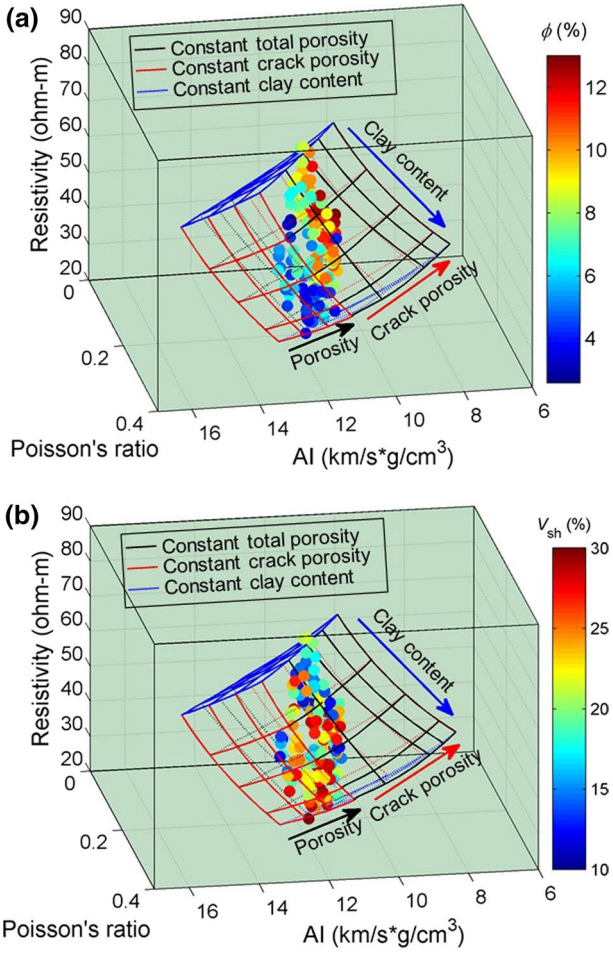

Fig. 20 3D RPT and well-log data: **a** porosity; **b** clay content

oil-producing section, and well log data from this layer (a clay content less than 30%) are selected to calibrate the AE RPT.

The study area is almost saturated with oil, so that full-oil saturation is assumed. The frequency is 10 kHz to match the sonic log data, and the radii of the crack and clay inclusions are set to 1 mm. As shown in Fig. 20, the well log data are projected onto the template, with the color bar denoting porosity (a) and clay content (b). The data are consistent with the RPTs, and the three attributes show the same trend with increasing porosity and clay content. Thus, a quantitative characterization of the reservoir properties can be obtained by superimposing the well log data on the template.

5.3 Application to Well Log Data

The three and two sandstone layers of Wells A and B are selected, respectively, to estimate the clay content, and the total and crack porosities. The impedance, Poisson's

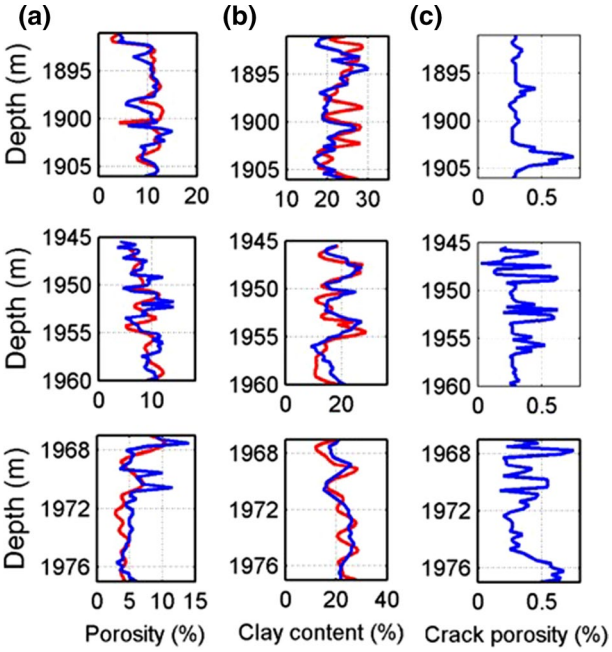

Fig. 21 Results for Well A; **a** porosity **b** clay content **c** crack porosity

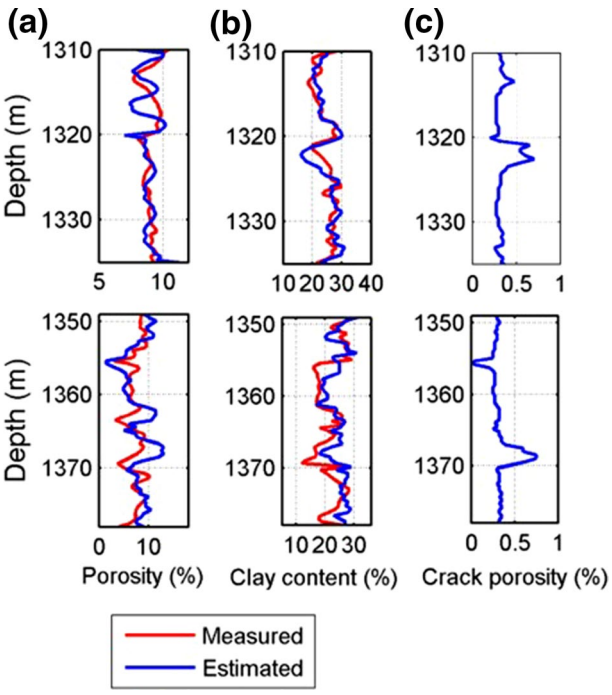

Fig. 22 Same as Fig. 21 but for Well B

ratio and resistivity are projected onto the RPT, the nearest grid of each data point is searched, and its reservoir properties are assigned to the data.

Figures 21 and 22 show the predictions and log interpretation for Wells A and B. The main ranges of clay content, total and crack porosities are 8–30%, 2–15% and 0–0.7%, respectively. The predicted curves are basically in agreement with the porosity and clay content of the two wells. It is clear that there is a good relation between porosity and crack porosity, and it is oppositely correlated with clay content. Formations with high total and crack porosities and low clay content have better pore space and connectivity, and higher hydrocarbon storage potential.

6 Conclusions

We have analyzed the properties of a tight-oil reservoir based on a joint acoustic-electrical petrophysical model. The rocks belong to the Yanchang Formation in the *Q* area of the Ordos Basin, whose core samples were characterized by X-ray diffraction and cast thin sections. Then, ultrasonic and resistivity experiments were performed at different confining pressures. A 3D rock-physics template has been built, based on Poisson's ratio, impedance and resistivity, and calibrated with the ultrasonic and well-log data. The template was applied to predict the properties of the reservoir. We conclude the following:

(1) The rocks have low porosity and permeability, with microcracks and high clay content, which highly affect their petrophysical behavior.
(2) Wave velocities and resistivity increase with effective pressure (crack density decreases), and the conductivity decreases. The combined effects of the stiff pores, cracks and clay minerals have to be considered to obtain reliable predictions.
(3) The good match between the proposed joint model and data on the basis of acoustic-electrical rock-physics templates shows that these can effectively be used to perform suitable interpretations involving tight rocks.

Appendix 1: The geometrical factors (*P*, *Q*)

The coefficients P and Q for ellipsoidal inclusions are given in Berryman (1980) and Mavko et al. (2009),

$$P = \tfrac{1}{3}T_1,\ Q = \tfrac{1}{5}\left(T_2 - \tfrac{1}{3}T_1\right), \tag{13}$$

with the pertinent scalars T_1 and T_2 given by,

$$T_1 = \tfrac{3F_1}{F_2}\ \ T_2 - \tfrac{1}{3}T_1 = \tfrac{2}{F_3} + \tfrac{1}{F_4} + \tfrac{F_4F_5+F_6F_7-F_8F_9}{F_2F_4}, \tag{14}$$

where

$$F_1 = 1 + G\left[\tfrac{3}{2}(g+\theta) - J\left(\tfrac{3}{2}g + \tfrac{5}{2}\theta - \tfrac{4}{3}\right)\right], \tag{15}$$

$$F_2 = 1 + G\left[1 + \frac{3}{2}(g+\theta) - \frac{J}{2}\left(\frac{3}{2}g + 5\theta\right)\right] + H(3-4J) + \frac{G}{2}(G+3H)(3-4J)\left[g + \theta - J\left(g - \theta + 2\theta^2\right)\right], \tag{16}$$

$$F_3 = 1 + G\left[1 - (g + \frac{3}{2}\theta) + J(g+\theta)\right], \tag{17}$$

$$F_4 = 1 + \frac{G}{4}\left[g + 3\theta - J(g-\theta)\right], \tag{18}$$

$$F_5 = G\left[-g + J\left(g + \theta - \frac{4}{3}\right) + H\theta(3-4J)\right], \tag{19}$$

$$F_6 = 1 + G\left[1 + g - J(g+\theta) + H(1-\theta)(3-4J)\right], \tag{20}$$

$$F_7 = 2 + \frac{G}{4}\left[3g + 9\theta - J(3g+5\theta)\right] + H\theta(3-4J), \tag{21}$$

$$F_8 = G\left[1 - 2J + \frac{g}{2}(J-1) + \frac{\theta}{2}(5J-3)\right] + H(1-\theta)(3-4J), \tag{22}$$

$$F_9 = G\left[(J-1)g - J\theta\right] + H\theta(3-4J), \tag{23}$$

with G, H and J given by

$$G = \frac{\mu_i}{\mu_m} - 1, \tag{24}$$

$$H = \frac{1}{3}\left(\frac{K_i}{K_m} - \frac{\mu_i}{\mu_m}\right), \tag{25}$$

$$J = \left[\frac{(1-2\nu_m)}{2(1-\nu_m)}\right], \tag{26}$$

where K_m, μ_m and ν_m are the bulk and shear moduli and Poisson's ratio of the host phase, respectively, K_i, and μ_i are the bulk and shear moduli of the phase i, and

$$\theta = \left\{ \begin{array}{l} \dfrac{\alpha}{\left(\alpha^2-1\right)^{3/2}}\left[\alpha\left(\alpha^2-1\right)^{1/2} - \cosh^{-1}\alpha\right] \\ \dfrac{\alpha}{\left(1-\alpha^2\right)^{3/2}}\left[\cos^{-1}\alpha - \alpha\left(1-\alpha^2\right)^{1/2}\right] \end{array} \right\}, \tag{27}$$

for prolate ($\alpha > 1$) and oblate ($\alpha < 1$) spheroids, respectively, the α is aspect ratio, and

$$g = \frac{\alpha^2}{1-\alpha^2}(3\theta - 2), \tag{28}$$

Appendix 2: The dispersion equation

The dispersion equation is given in Sun et al. (2016) and Zhang et al. (2017). The plane-wave analysis was performed by substituting a time harmonic kernel $e^{i(\omega t - k\cdot\mathbf{x})}$ into Eq. (4). Then the complex wave number k can be obtained as

$$\begin{vmatrix} a_{11}k^2+b_{11} & a_{12}k^2+b_{12} & a_{13}k^2+b_{13} & a_{14}k^2+b_{14} \\ a_{21}k^2+b_{21} & a_{22}k^2+b_{22} & a_{23}k^2+b_{23} & a_{24}k^2+b_{24} \\ a_{31}k^2+b_{31} & a_{32}k^2+b_{32} & a_{33}k^2+b_{33} & a_{34}k^2+b_{34} \\ a_{41}k^2+b_{41} & a_{42}k^2+b_{42} & a_{43}k^2+b_{43} & a_{44}k^2+b_{44} \end{vmatrix} = 0, \tag{29}$$

and

$$\begin{aligned}
a_{11} &= A + 2N + \left(Q_1\phi_2 - Q_2\phi_1\right)M_0^{(12)} + \left(Q_2\phi_3 - Q_3\phi_2\right)M_0^{(23)}, \\
a_{12} &= Q_1 + \left(Q_1\phi_2 - Q_2\phi_1\right)M_1^{(12)} + \left(Q_2\phi_3 - Q_3\phi_2\right)M_1^{(23)}, \\
a_{13} &= Q_2 + \left(Q_1\phi_2 - Q_2\phi_1\right)M_2^{(12)} + \left(Q_2\phi_3 - Q_3\phi_2\right)M_2^{(23)}, \\
a_{14} &= Q_3 + \left(Q_1\phi_2 - Q_2\phi_1\right)M_3^{(12)} + \left(Q_2\phi_3 - Q_3\phi_2\right)M_3^{(23)}, \\
a_{21} &= Q_1 + \phi_2 R_1 M_0^{(12)}, \quad a_{22} = R_1 + \phi_2 R_1 M_1^{(12)}, \\
a_{23} &= \phi_2 R_1 M_2^{(12)}, \quad a_{24} = \phi_2 R_1 M_3^{(12)}, \\
a_{31} &= Q_2 - R_2\left(\phi_1 M_0^{(12)} - \phi_3 M_0^{(23)}\right), \quad a_{32} = -R_2\left(\phi_1 M_1^{(12)} - \phi_3 M_1^{(23)}\right), \\
a_{33} &= R_2\left(1 - \phi_1 M_2^{(12)} + \phi_3 M_2^{(23)}\right), \quad a_{34} = R_2\left(-\phi_1 M_3^{(12)} + \phi_3 M_3^{(23)}\right), \\
a_{41} &= Q_3 - \phi_2 R_3 M_0^{(23)}, \quad a_{42} = -\phi_2 R_3 M_1^{(23)}, \\
a_{43} &= -\phi_2 R_3 M_2^{(23)}, \quad a_{44} = R_3\left(1 - \phi_2 M_3^{(23)}\right), \\
b_{11} &= -\rho_{00}\omega^2 + i\omega\left(b_1 + b_2 + b_3\right), \quad b_{12} = -\rho_{01}\omega^2 - i\omega b_1, \\
b_{13} &= -\rho_{02}\omega^2 - i\omega b_2, \quad b_{14} = -\rho_{03}\omega^2 - i\omega b_3, \\
b_{21} &= -\rho_{01}\omega^2 - i\omega b_1, \quad b_{22} = -\rho_{11}\omega^2 + i\omega b_1, b_{23} = b_{24} = 0, \\
b_{31} &= -\rho_{02}\omega^2 - i\omega b_2, \quad b_{33} = -\rho_{22}\omega^2 + i\omega b_2, b_{32} = b_{34} = 0, \\
b_{41} &= -\rho_{03}\omega^2 - i\omega b_3, \quad b_{44} = -\rho_{33}\omega^2 + i\omega b_3, b_{42} = b_{43} = 0,
\end{aligned} \tag{30}$$

where the Biot dissipation coefficients (Biot 1962 and Sun et al. 2016) and the permeabilities of the three phases (Vaughan et al. 1986 and Mavko et al. 2009),

$$\begin{aligned}
&b_1 = \phi_1\phi_{10}\frac{\eta_f}{\kappa_1}, \; b_2 = \phi_2\phi_{20}\frac{\eta_f}{\kappa_2}, \; b_3 = \phi_3\phi_{30}\frac{\eta_f}{\kappa_3}, \\
&\kappa_1 = DR_{12}^2\phi_1^3, \; \kappa_2 = \frac{\kappa_0\phi_2^3}{\left(1-\phi_2\right)^2}, \quad \kappa_3 = \frac{\kappa_0\phi_3^3}{\left(1-\phi_3^2\right)},
\end{aligned} \tag{31}$$

where $D = 50$ and $\kappa_0 = 75.54$ mdarcy, and

$$
\begin{aligned}
S_{12} =& \frac{-\phi_1\phi_2^2R_{12}^2\omega\left(\rho_f\omega\left(1/5+\phi_{10}/\phi_{20}\right)+i\left(\eta/\left(5\kappa_1\right)+\eta/\kappa_2\right)\phi_{10}\right)}{3}-\phi_2^2R_1-\phi_1^2R_2,\\
S_{23} =& \frac{-\phi_3\phi_2^2R_{23}^2\omega\left(\rho_f\omega\left(1/5+\phi_{30}/\phi_{20}\right)+i\left(\eta/\left(5\kappa_3\right)+\eta/\kappa_2\right)\phi_{30}\right)}{3}-\phi_3^2R_2-\phi_2^2R_3,\\
M_0^{(12)} =& \frac{\left(Q_1\phi_2-Q_2\phi_1\right)/S_{12}+\phi_1\phi_3R_2\left(Q_2\phi_3-Q_3\phi_2\right)/\left(S_{12}S_{23}\right)}{1+\left(\phi_1\phi_3R_2\right)^2/\left(S_{12}S_{23}\right)},\\
M_1^{(12)} =& \frac{\phi_2R_1/S_{12}}{1+\left(\phi_1\phi_3R_2\right)^2/\left(S_{12}S_{23}\right)},\\
M_2^{(12)} =& \frac{-\phi_1R_2/S_{12}+\phi_1\phi_3^2R_2^2/\left(S_{12}S_{23}\right)}{1+\left(\phi_1\phi_3R_2\right)^2/\left(S_{12}S_{23}\right)},\quad M_3^{(12)}=\frac{-\phi_1\phi_2\phi_3R_2R_3/\left(S_{12}S_{23}\right)}{1+\left(\phi_1\phi_3R_2\right)^2/\left(S_{12}S_{23}\right)},\\
M_0^{(23)} =& \left(-M_0^{(12)}\phi_1\phi_3R_2+Q_2\phi_3-Q_3\phi_2\right)/S_{23},\quad M_1^{(23)}=-M_1^{(12)}\phi_1\phi_3R_2/S_{23},\\
M_2^{(23)} =& \left(-M_2^{(12)}\phi_1\phi_3R_2+\phi_3R_2\right)/S_{23},\quad M_3^{(23)}=\left(-M_3^{(12)}\phi_1\phi_3R_2-\phi_2R_3\right)/S_{23}.
\end{aligned}
\tag{32}
$$

The stiffness and density coefficients are

$$
\begin{aligned}
A=(1-\phi)K_s-\frac{2}{3}N-\frac{K_s}{K_f}\left(Q_1+Q_2+Q_3\right),\quad N=\mu_b,\\
Q_1=\frac{\phi_1\beta_1K_s}{\beta_1+\gamma},\quad Q_2=\frac{\phi_2K_s}{1+\gamma},\quad Q_3=\frac{\phi_3K_s}{\beta_1\gamma+1},\\
R_1=\frac{\phi_1K_f}{\beta_1/\gamma+1},\quad R_2=\frac{\phi_2K_f}{1+1/\gamma},\quad R_3=\frac{\phi_3K_f}{1/\beta_1\gamma+1},\\
\gamma=\frac{K_s}{K_f}\frac{\phi_1\beta_1+\phi_2+\phi_3/\beta_2}{(1-\phi)-K_b/K_s},
\end{aligned}
\tag{33}
$$

$$
\begin{aligned}
\rho_{11}=\tfrac{1}{2}\phi_1\rho_f\left(1+\tfrac{1}{\phi_{10}}\right),\ \rho_{22}=\tfrac{1}{2}\phi_2\rho_f\left(1+\tfrac{1}{\phi_{20}}\right),\ \rho_{33}=\tfrac{1}{2}\phi_3\rho_f\left(1+\tfrac{1}{\phi_{30}}\right),\\
\rho_{01}=\phi_1\rho_f-\rho_{11},\ \rho_{02}=\phi_2\rho_f-\rho_{22},\ \rho_{03}=\phi_3\rho_f-\rho_{33},\\
\rho_{00}=v_1(1-\phi_{10})\rho_{s1}+v_2(1-\phi_{20})\rho_{s2}+v_3(1-\phi_{30})\rho_{sh}-\rho_{01}-\rho_{02}-\rho_{03},
\end{aligned}
\tag{34}
$$

where K_s, K_b and K_f are the bulk moduli of the mineral mixture, skeleton and fluid, respectively, ρ_{s1}, ρ_{s2} and ρ_{sh} are the mineral densities corresponding to the three phases, ρ_f is the fluid density, and

$$
\begin{aligned}
\beta_1=\frac{Q_1R_2}{Q_2R_1}=\frac{\phi_{20}}{\phi_{10}}\left[\frac{1/K_{s1}-\left(1-\phi_{10}\right)/K_{b1}}{1/K_{s2}-\left(1-\phi_{20}\right)/K_{b2}}\right],\\
\beta_2=\frac{Q_2R_3}{Q_3R_2}=\frac{\phi_{30}}{\phi_{20}}\left[\frac{1/K_{s2}-\left(1-\phi_{20}\right)/K_{b2}}{1/K_{sh}-\left(1-\phi_{30}\right)/K_{b3}}\right].
\end{aligned}
\tag{35}
$$

where K_{b1}, K_{b2} and K_{b3} are the skeleton bulk moduli of the crack inclusions, host and clay inclusions, respectively, and K_{s1}, K_{s2} and K_{sh} are the mineral bulk moduli corresponding to the three phases.

Acknowledgements The authors are grateful to the Editor in Chief and anonymous reviewers for their valuable comments. The authors appreciate the help of Dr. Han Xuehui for the experimental tests and helpful discussions. This work is supported by the National Natural Science Foundation of China (Grant No. 41974123, No. 42174161), the Jiangsu Innovation and Entrepreneurship Plan and the Jiangsu Province Science Fund for Distinguished Young Scholars (Grant No. BK20200021).

Declarations

Conflict of interest The authors declare that they have no known competing financial interests or personal relationships that could have appeared to influence the work reported in this paper.

References

Amalokwu K, Falcon-Suarez IH (2021) Effective medium modeling of pressure effects on the joint elastic and electrical properties of sandstones. J Petrol Sci Eng 202:108540

Anguy Y, Bernard D, Ehrlich R (1996) Towards realistic flow modelling. Creation and evaluation of two-dimensional simulated porous media: an image analysis approach. Surv Geophys 17(3):265–287

Archie GE (1942) The electrical resistivity log as an aid in determining some reservoir characteristics. Trans AIME 146(5):4–62. https://doi.org/10.2118/942054-G

Attias E, Amalokwu K, Watts M, Falcon-Suarez IH, North L, Hu GW, Minshull TA (2020) Gas hydrate quantification at a pockmark offshore Norway from joint effective medium modelling of resistivity and seismic velocity. Mar Pet Geol 113:104151

Bakar WZW, Saaid IM, Ahmad MR, Amir Z, Mahat SQA (2019) Derivation of formation factor in shaly sandstone with geometry and clay conductivity effects. J Petrol Sci Eng 182:106359

Batzle M, Wang Z (1992) Seismic properties of pore fluids. Geophysics 57:1396–1408

Ba J, Ma R, Carcione J, Picotti S (2019) Ultrasonic wave attenuation dependence on saturation in tight oil siltstones. J Petrol Sci Eng 179:1114–1122. https://doi.org/10.1016/j.petrol.2019.04.099

Ba J, Xu W, Fu L, Carcione J, Zhang L (2017) Rock anelasticity due to patchy-saturation and fabric heterogeneity: a double-double porosity model of wave propagation. J Geophys Res Solid Earth 122(3):1949–1976. https://doi.org/10.1002/2016JB013882

Behmanesh H, Hamdi H, Clarkson CR, Thompson JM, Anderson DM (2018) Analytical modeling of linear flow in single-phase tight oil and tight gas reservoirs. J Petrol Sci Eng 171:1084–1098

Berryman JG (1980) Long-wavelength propagation in composite elastic media. J Acoust Soc Am 68(6):1809–1831

Berryman JG (1992) Single-scattering approximations for coefficients in Biot's equations of poroelasticity. Acoust Soc Am J 91(2):551–571

Berryman JG (1995) Mixture theories for rock properties. Rock Phys Phase Relat A Handb Phys Constants 3:205–228

Biot MA (1962) Mechanics of deformation and acoustic propagation in porous media. J Appl Phys 33(4):1482–1498

Carcione JM (2014) Wavefields in real media. In: Theory and numerical simulation of wave propagation in anisotropic, anelastic, porous and electromagnetic media, 3rd edn. Amsterdam, Netherlands: Elsevier

Carcione JM, Ursin B, Nordskag JI (2007) Cross-property relations between electrical conductivity and the seismic velocity of rocks. Geophysics 72(5):E193–E204

Cilli P, Chapman M (2018) Modelling the elastic and electrical proper-ties of rocks with complex pore geometries. In: 80th annual international conference and exhibition, EAGE, extended abstracts. https://doi.org/10.3997/2214-4609.201801407

Cilli P, Chapman M (2020) The power-law relation between inclusion aspect ratio and porosity: implications for electrical and elastic modeling. J Geophys Res Solid Earth 125(5):1–25

Cilli P, Chapman M (2021) Linking elastic and electrical properties of rocks using cross-property DEM. Geophys J Int 225:1812–1823

Cole KS, Cole RH (1941) Dispersion and absorption in dielectrics, vol. I: alternating current field. J Chem Phys 9:341–351

David EC, Zimmerman RW (2012) Pore structure model for elastic wave velocities in fluid-saturated sandstones. J Geophys Res Solid Earth 117: B07210. https://doi.org/10.1029/2012JB009195

Dutilleul J, Bourlange S, Géraud Y, Stemmelen D (2020) Porosity, pore structure, and fluid distribution in the sediments entering the northern Hikurangi margin, New Zealand. J Geophys Res Solid Earth 125:e2020JB020330. https://doi.org/10.1029/2020JB020330

Falcon-Suarez IH, Amalokwu K, Delgado-Martin J, Callow B, Robert K, North L et al (2019) Comparison of stress-dependent geophysical, hydraulic and mechanical properties of synthetic and natural sandstones for reservoir characterization and monitoring studies. Geophys Prospect 67(4):784–803

Fan J, Shi J, Wan X, Xie Q, Wang C (2021) Classification evaluation method for Chang 7 oil group of Yanchang formation in Ordos basin. J Pet Explor Prod Technol 12(3):825–834

Fliedner C, French ME (2021) Pore and mineral fabrics control the elastic wave velocities of metapelite with implications for subduction zone tomography. J Geophys Res Solid Earth 126:e2021JB022361. https://doi.org/10.1029/2021JB022361

Gabàs A, Macau A, Benjumea B, Queralt P, Ledo J, Figueras S, Marcuello A (2016) Joint audio-magnetotelluric and passive seismic imaging of the Cerdanya Basin. Surv Geophys 37:897–921. https://doi.org/10.1007/s10712-016-9372-4

Gao S, Yang Y, Liao G, Xiong W, Liu H, Shen R, An W (2022) Experimental research on inter-fracture asynchronous injection-production cycle for a horizontal well in a tight oil reservoir. J Petrol Sci Eng 208:109647

Ghasemi S, Khamehchiyan M, Taheri A, Nikudel MR, Zalooli A (2020) Crack evolution in damage stress thresholds in different minerals of granite rock. Rock Mech Rock Eng 53(3):1163–1178

Ghanizadeh A, Clarkson C, Aquino S, Ardakani O, Sanei H (2015) Petrophysical and geomechanical characteristics of Canadian tight oil and liquid-rich gas reservoirs: pore network and permeability characterization. Fuel 153:664–681. https://doi.org/10.1016/j.fuel.2015.03.020

Gomes OA, Yednak CAR, de Almeida RR, Teixeira-Souza RT, Evangelista LR (2017) Elastic anisotropy effects on the electrical responses of a thin sample of nematic liquid crystal. Phys Rev E 95(3):032704

Gomez CT, Dvorkin J, Vanorio T (2010) Laboratory measurements of porosity, permeability, resistivity, and velocity on Fontainebleau sandstones. Geophysics 75(6):E191–E204

Hacikoylu P, Dvorkin J, Mavko G (2006) Resistivity-velocity transforms revisited. Lead Edge 25(8):1006–1009

Han T, Best A, Sothcott J, MacGregor L (2011) Joint elastic-electrical properties of reservoir sandstones and their relationships with petrophysical parameters. Geophys Prospect 59:518–535

Han T, Clennell M, Cheng A, Pervukhina M (2016) Are self-consistent models capable of jointly modeling elastic velocity and elec-trical conductivity of reservoir sandstones? Geophysics 81(4):D377–D382. https://doi.org/10.1190/geo2015-0690.1

Han T, Wei Z, Li F (2020) How the effective pore and grain shapes are correlated in Berea sandstones: implications for joint elastic-electrical modeling. Geophysics 85(3):MR147–MR154

Han XH, Kuang LC, He Y, Tao G, Ke SZ (2005) A view of the experimental study on rock'electric property. Prog Geophys 20(2):348–356

Hashin Z, Shtrikman S (1962) A variational approach to the theory of effective magnetic permeability of multiphase materials. J Appl Phys 33:3125–3131

Hashin Z, Shtrikman S (1963) A variational approach to the elastic behavior of multiphase materials. J Mech Phys Solids 11(2):127–140. https://doi.org/10.1016/0022-5096(63)90060-7

Heinson G (1999) Electromagnetic studies of the lithosphere and asthenosphere. Surv Geophys 20(3):229–255

Heise W, Ellis S (2016) On the coupling of geodynamic and resistivity models: a progress report and the way forward. Surv Geophys 37(1):81–107

Iqbal MA, Rezaee R, Smith G, Ekundayo JM (2021) Shale lithofacies controls on porosity and pore structure: an example from Ordovician Goldwyer formation, Canning basin, Western Australia. J Nat Gas Sci Eng 89:103888

Iwamori H, Ueki K, Hoshide T, Sakuma H, Ichiki M, Watanabe T et al (2021) Simultaneous analysis of seismic velocity and electrical conductivity in the crust and the uppermost mantle: a forward model and inversion test based on grid search. J Geophys Res Solid Earth 126:e2021JB022307. https://doi.org/10.1029/2021JB022307

Jensen EH, Gelius LJ, Johansen TA, Wang Z (2013) Consistent joint elastic-electrical differential effective-medium modelling of compacting reservoir sandstones. Geophys Prospect 61(4):788–802

Ji X, Wang H, Ge Y, Liang J, Xu X (2022) Empirical mode decomposition-refined composite multiscale dispersion entropy analysis and its application to geophysical well log data. J Petrol Sci Eng 208:109495

Kathel P, Mohanty KK (2013) Wettability alteration in a tight oil reservoir. Energy Fuels 27(11):6460–6468

Kazatchenko E, Markov M, Mousatov A (2004) Joint modeling of acoustic velocities and electrical conductivity from unified microstructure of rocks. J Geophys Res 109:B01202. https://doi.org/10.1029/2003JB002443

Kozlovskaya E, Hjelt SE (2000) Modeling of elastic and electrical properties of solid-liquid rock system with fractal microstructure. Phys Chem Earth Part A 25(2):195–200
Kumar S, Mendhe VA, Kamble AD, Varma AK, Mishra DK, Bannerjee M, Prasad AK (2019) Geochemical attributes, pore structures and fractal characteristics of Barakar shale deposits of Mand-Raigarh Basin, India. Mar Pet Geol 103:377–396
Leger M, Luquot L (2021) Importance of microstructure in carbonate rocks: laboratory and 3D-imaging petrophysical characterization. Appl Sci 11(9):3784
Leveaux J, Poupon A (1971) Evaluation of water saturation in shaly formations. Log Anal 12(04): 3–8
Lin R, Yu Z, Zhao J, Dai C, Sun Y, Ren L, Xie M (2022) Experimental evaluation of tight sandstones reservoir flow characteristics under CO_2–Brine–Rock multiphase interactions: a case study in the Chang 6 layer, Ordos Basin. China Fuel 309:122167
Liu Q, Li P, Jin Z, Sun Y, Hu G, Zhu D, Liu J (2021) Organic-rich formation and hydrocarbon enrichment of lacustrine shale strata: a case study of Chang 7 Member. Sci China Earth Sci 65, 118–138. https://doi.org/10.1007/s11430-021-9819-y
Lu M, Cao H, Sun W, Yan X, Yang Z, Xu Y, Wang Z, Ouyang M (2019) Quantitative prediction of seismic rock physics of hybrid tight oil reservoirs of the Permian Lucaogou formation, Junggar Basin, Northwest China. J Asian Earth Sci 178:216–223
Ma R, Ba J, Carcione J, Zhou X, Li F (2019) Dispersion and attenuation of compressional waves in tight oil reservoirs: experiments and simulations. Appl Geophys 16(1):33–45. https://doi.org/10.1007/s11770-019-0748-3
Ma C, Zhao X, Yang T, Jiang W, Guo B, Han G, Zhu H (2021) Mineralogy, organic geochemistry, and microstructural characterization of lacustrine Shahejie Formation, Qikou Sag, Bohai Bay Basin: contribution to understanding microcosmic storage mechanism of shale oil. J Pet Sci Eng 209:109843
Mahanta B, Vishal V, Ranjith PG, Singh TN (2020) An insight into pore-network models of high-temperature heat-treated sandstones using computed tomography. J Nat Gas Sci Eng 77:103227
Mavko G, Mukerji T, Dvorkin J (2009) The rock physics handbook: tools for seismic analysis of porous media. Cambridge University Press, Cambridge
Mansoor N, Slater L (2007) On the relationship between iron concentration and induced polarization in marsh soils. Geophysics 72(1):A1–A5
Nover G (2005) Electrical properties of crustal and mantle rocks–a review of laboratory measurements and their explanation. Surv Geophys 26(5):593–651
Ozotta O, Liu K, Gentzis T, Carvajal-Ortiz H, Liu B, Rafieepour S, Ostadhassan M (2021) Pore structure alteration of organic-rich shale with Sc-CO_2 exposure: the Bakken formation. Energy Fuels 35(6):5074–5089
Pang M, Ba J, Carcione J, Picotti S, Zhou J, Jiang R (2019) Estimation of porosity and fluid saturation in carbonates from rock-physics templates based on seismic Q. Geophysics 84(6):M25–M36. https://doi.org/10.1190/geo2019-0031.1
Pang M, Ba J, Carcione J, Zhang L, Ma R, Wei Y (2021a) Seismic identification of tight-oil reservoirs by using 3D rock-physics templates. J Pet Sci Eng 201:108476
Pang M, Ba J, Carcione JM, Saenger EH (2021b) Elastic-electrical rock-physics template for the characterization of tight-oil reservoir rocks. Lithosphere 2021:3341849
Pelton WH, Ward SH, Hallof PG, Sill WR, Nelson PH (1978) Mineral discrimination and removal of inductive coupling with multifrequency IP. Geophysics 43:588–609
Pride SR, Berryman JG, Commer M, Nakagawa S, Newman GA, Vasco DW (2017) Changes in geophysical properties caused by fluid injection into porous rocks: analytical models. Geophys Prospect 65(3):766–790
Revil A, Coperey A, Mao D, Abdulsamad F, Ghorbani A, Rossi M, Gasquet D (2018) Induced polarization response of porous media with metallic particles-part 8: influence of temperature and salinity. Geophysics 83(6):E435–E456
Shen H, Li X, Li Q (2022) Influence of the microstructure on stress-dependent P-wave anisotropy in sandstone. Geophys J Int 228(2):876–892
Siitari-Kauppi M, Lindberg A, Hellmuth KH, Timonen J, Väätäinen K, Hartikainen J, Hartikainen K (1997) The effect of microscale pore structure on matrix diffusion—a site-specific study on tonalite. J Contam Hydrol 26(1–4):147–158
Solano NA, Soroush M, Clarkson CR, Krause FF, Jensen JL (2017) Modeling core-scale permeability anisotropy in highly bioturbated "tight oil" reservoir rocks. Comput Geosci 21(3):567–593
Sun W, Ba J, Carcione JM (2016) Theory of wave propagation in partially saturated double-porosity rocks: a triple-layer patchy model. Geophys J Int 205(1):22–37. https://doi.org/10.1093/gji/ggv551
Sun H, Duan L, Liu L, Fan W, Fan D, Yao J, Zhao J (2019) The influence of micro-fractures on the flow in tight oil reservoirs based on pore-network models. Energies 12(21):4104

Vaughan PJ, Moore DE, Morrow CA, Byerlee JD (1986) Role of cracks in progressive permeability reduction during flow of heated aqueous fluids through granite. J Geophys Res Solid Earth 91(B7):7517–7530

Wang KW, Sun JM, Geng SC, Wu JL (2006) Percolation network study of shale effects on rock electrical properties under different salinity. Chin J Geophys 49(6):1710–1717

Wang S, Tan M, Wang X, Zhang L (2022) Microscopic response mechanism of electrical properties and saturation model establishment in fractured carbonate rocks. J Petrol Sci Eng 208:109429

Wu M, Gao K, Liu J, Song Z, Huang X (2022) Influence of rock heterogeneity on hydraulic fracturing: a parametric study using the combined finite-discrete element method. Int J Solids Struct 234:111293

Wu Y, Lin C, Yan W, Liu Q, Zhao P, Ren L (2020) Pore-scale simulations of electrical and elastic properties of shale samples based on multicomponent and multiscale digital rocks. Mar Pet Geol 117:104369

Zhang L, Ba J, Fu L, Carcione JM, Cao C (2019) Estimation of pore microstructure by using the static and dynamic moduli. Int J Rock Mech Min Sci 113:24–30

Zhang L, Ba J, Yin W, Sun W, Tang J (2017) Seismic wave propagation equations of conglomerate reservoirs: a triple-porosity structure model. Chin J Geophys (in Chinese) 60(3):1073–1087

Zhang L, Ba J, Carcione JM (2021) Wave propagation in infinituple-porosity media. J Geophy Res Solid Earth 126(4):e2020JB021266

Zhang L, Ba, J, Carcione JM, Wu C (2022) Seismic wave propagation in partially saturated rocks with a fractal distribution of fluid-patch size. J Geophy Res Solid Earth 127(2):e2021JB023809

Publisher's Note Springer Nature remains neutral with regard to jurisdictional claims in published maps and institutional affiliations.